Development and assessment of the physical-biogeochemical ocean regional model in the Northwest Pacific: NPRT v1.0 (ROMS v3.9–TOPAZ v2.0)

Daehyuk Kim[1], Hyun-Chae Jung[4], Jae-Hong Moon[1,2,3], Na-Hyeon Lee[3]

[1] *Center for Sea Level Changes, Jeju National University, Jeju, 63243, Republic of Korea*

[2] *Department of Earth and Marine Sciences, Jeju National University, Jeju, 63243, Republic of Korea*

[3] *Faculty of Earth and Marine Convergence, Earth and Marine Science Major, Jeju National University, Jeju, 63243, Republic of Korea*

[4] *Department of Earth and Environmental Sciences, Jeonbuk National University, Jeonju, 54896, Republic of Korea*

Corresponding author: Jae-Hong Moon, jhmoon@jejunu.ac.kr

16   Abstract

17 The Northwest Pacific is characterized by the presence of the warm and nutrient-depleted Kuroshio
18 Current and the cold and nutrient-enriched Oyashio Current. In this region, surface primary production
19 leads to increased nutrient consumption and CO_2 exchange. The Yellow and East China Seas (YECS)
20 are predominantly influenced by freshwater input. A high resolution regional numerical model tailored
21 to the specific features of each area is required to reproduce the different characteristics of each region.
22 Therefore, to accurately analyze the physical and biogeochemical system, this study developed a new
23 coupled physical-biogeochemical model combining the three-dimensional Regional Ocean Modeling
24 System (ROMS) and the Generic Ocean Turbulence Model Tracers of Phytoplankton with Allometric
25 Zooplankton (TOPAZ) for the Northwest Pacific, including the YECS. The simulated physical and
26 biogeochemical variables in the ROMS–TOPAZ (NPRT) were evaluated by comparing them with
27 available observational data. NPRT successfully simulated the seasonal variability of chlorophyll and
28 nutrients, capturing two peaks in spring and autumn, which were not captured by the CMIP6 data.
29 Particularly in the YECS, NPRT effectively represented the high phytoplankton biomass driven by
30 riverine effect, which is difficult to reproduce in global biogeochemical model with low-resolution.
31 However, NPRT still exhibits significant biases in the subarctic region and marginal seas. To minimize
32 the uncertainties in biogeochemical variables, it is necessary to refine the initial and boundary
33 conditions, adjust parameters, and apply discharge forcing based on observational data. Despite these
34 limitations, NPRT is an important tool for studying the interaction between ocean physics and
35 biogeochemistry at a high resolution.

37 ## 1. Introduction

38   The pronounced global climate change tends in the 21st century have increased interest in various
39 research fields, including physical oceanography, atmospheric science, and biogeochemistry. The recent
40 exponential increase in computer resources has enabled us to consider simultaneously two or more
41 disciplines and conduct numerical studies on complex interactions among various fields. The ocean
42 biogeochemical processes are among the most important fields for understanding Earth's carbon and
43 ecosystem cycles, as well as the global climate system (Reid et al., 2009; Kang et al., 2017; Park et al.,
44 2014, 2018, Lee et al., 2022). Previous studies utilized Earth system models to analyze ocean
45 biogeochemistry, climate feedback, and the carbon cycle (Kang et al., 2017; Park et al., 2018; 2019). In
46 particular, significant efforts have been made to analyze physical–biogeochemical features at the global
47 scale as well as at regional scales (Hauri et al., 2020; Zhao et al., 2021; Wu et al., 2023; Na et al., 2024).

The North Pacific is a key region where the biological carbon pump occurs effectively (Chierici et al., 2006; Takahashi et al., 2009). Low-frequency physical and ecological variabilities in the North Pacific are closely related to various climatological variability patterns, such as the Pacific Decadal Oscillation (PDO) and El Niño–Southern Oscillation (ENSO). Numerous studies have been conducted on the responses of ecosystems to climatic and environmental conditions influenced by these long-term climatological variability patterns, especially in the Northeast Pacific (Overland et al., 2008; Yatsu et al., 2013; Ma et al., 2020). However, in the Northwest Pacific, including marginal seas, regional-scale oceanographic and ecological variabilities are independent across regions and show relatively weak linkages to climatological variability patterns, such as the PDO and ENSO (Jung et al., 2017; Ma et al., 2020). In particular, the Northwest Pacific is known as the Kuroshio–Oyashio Confluence Region (142–160° E, 35–40° N; Kawai, 1972; Hanawa and Mitsudera, 1987); the Oyashio Current is formed from the East Kamchatka Current, flowing southwestward along the Hokkaido coast while mixing with the Okhotsk Sea Mode Water, and the Kuroshio Current flows northeastward along the east of Japan, originating from Luzon Island (Nitani, 1972). Therefore, this region is known for the convergence of distinct water properties, resulting in a complex frontal structure, thermohaline mixing, and significant variability in the upper layer circulation (Qiu, 2001; Yasuda, 2003; Taguchi et al., 2007). Specifically, the water mass of the Oyashio Current has low temperature and low salinity, i.e., lower than 7 °C and 33.7 psu at a depth of 100 m (Kawai, 1972). Conversely, the water mass of the Kuroshio Current has a temperature higher than 14 °C and salinity higher than 34.7 psu (Nitani, 1972; Wang et al., 2022). In this region, the biogeochemical characteristics also exhibit significant regional differences. The cyclonic subarctic gyre, located west of the Oyashio Current, is characterized by high nutrient levels and low chlorophyll concentration (Taniguchi, 1999). Conversely, the anticyclonic tropical gyre, situated in the Kuroshio Current, is characterized by low nutrient levels (Siswanto et al., 2015). The interaction between gyres with distinct biogeochemical characteristics results in increased nutrient availability and the simulation of high phytoplankton biomass (Shiozaki et al., 2014). Consequently, the Northwest Pacific has been extensively studied from the perspectives of hydrography, climate change, nutrient transport, the carbon cycle, phytoplankton production, and community structure in relation to external conditions (Okamoto et al., 2010; Kuroda et al., 2019; Wang et al., 2021).

The Northwest Pacific is an important region for understanding the global carbon cycle and enhancing its predictability. Many previous studies have analyzed the carbon cycle, ecosystems, and future climate change using low-resolution global climate models with biogeochemical modules (Park et al., 2014; Jung et al., 2020; Hauri et al., 2020; Lee et al., 2022). However, coupled physical–biogeochemical ocean models with low horizontal resolutions involve limitations regarding accurately reproducing and analyzing the characteristics of oceanic environmental systems particularly the

82   physical–biogeochemical factors in regional areas. Therefore, in this study, to accurately understand the

83   physical–biogeochemical processes at the regional scale and address uncertainties, a regional ocean

84   model and a biogeochemical model were coupled at a high resolution. Specifically, we employed the

85   Generic Ocean Turbulence Model–Tracers of Phytoplankton with Allometric Zooplankton (TOPAZ)

86   developed by the US National Oceanic and Atmospheric Administration's Geophysical Fluid Dynamics

87   Laboratory (GFDL), in conjunction with the Regional Ocean Modeling System (ROMS).

88   This study introduces a new high-resolution coupled physical-biogeochemical model, named the

89   "Northwest Pacific ROMS–TOPAZ model version 1.0 (hereafter NPRT)", which is a valuable tool for

90   not only understanding the interactions between physical and biogeochemical processes but also for

91   predicting the future ocean carbon system. We describe and evaluate the simulation results of the

92   coupled physical–biogeochemical model (NPRT) through comparison with available observational data.

93   Sections 2.1 and 2.2 describe the characteristics of the models used in this study, and Section 2.3 and

94   2.4 elaborate on the developed NPRT, the methodology behind it, and the specific model design for the

95   study area. In section 3, the model results are evaluated using observations of physical and

96   biogeochemical variables, such as sea surface height (SSH), salinity, chlorophyll, nutrients, dissolved

97   inorganic carbon (DIC), and dissolved oxygen (DO). In addition, we analyze the characteristics of the

98   physical–biogeochemistry regional ocean model with high resolution. Finally, a summary is presented

99   in section 4.

100

2. Data and model

2.1 Physical Ocean model (ROMS v3.9)

103   For conducting the physical–biogeochemical model coupling in this study, we employed ROMS

104   version 3.9 (hereafter ROMS; Song and Haidvogel, 1994), which is a popular physical regional ocean

105   model. ROMS is a three-dimensional primitive-equation physical ocean model that uses hydrostatic

106   and Boussinesq approximations. The horizontal grid system is the Arakawa-C grid system, which

107   enhances computational stability and efficiency (Arakawa and Lamb, 1977). The vertical coordinate

108   system is the S-coordinate (stretched terrain-following coordinate), which combines the advantages of

109   implementing the z-coordinate for the planetary boundary layer (PBL) and the σ-coordinate for the

110   bottom boundary layer. In this way, it allows for accurate analyses of physical phenomena in the

111   thermocline or bottom boundary layer, while reducing pressure gradient errors that are sensitive to the

112   terrain (Song and Wright, 1998; Shchepetkin and McWilliams, 2003).

113   ROMS can utilize horizontal advection schemes, such as second-, and fourth-order centered

114 differences and a third-order upstream scheme. Various options are available for vertical mixing,

115 including the K-profile parameterization (KPP; Large et al., 1994), M–Y (Mellor and Yamada, 1982),

116 Generic Length Scale (GLS; Umlauf and Burchard, 2003). In addition, bulk parameterization involving

117 the wind, sensible heat flux, and latent heat flux provides better calculations of the heat budget changes,

118 which is essential for elucidating the atmosphere–ocean interactions (Fairall et al., 1996). For more

119 information on ROMS, we refer to Shchepetkin and McWilliams (2005) and McWilliams (2009).

2.2 Biogeochemical model (TOPAZ v2.0)

121 TOPAZ version 2.0 (hereafter TOPAZ) is a biogeochemical module that simulates the cycles of

122 carbon, nitrogen, phosphorus, silicon, iron, DO, and lithogenic material, while also considering the

123 growth cycles of the zooplankton and phytoplankton. In biogeochemical processes, phytoplankton

124 members are categorized based on their sizes into small and large, including the nitrogen-fixing

125 diazotrophs. Overall, TOPAZ handles a total of 30 prognostic and 11 diagnostic tracers, and the state

126 variable C in various tracers reproduced in TOPAZ can be calculated using the following continuity

127 equation to describe local changes.

128 $$\frac{\partial C}{\partial t} = -\nabla \cdot \tilde{v} C + \nabla K \nabla C + S_c, \qquad (1)$$

129

130 where $\tilde{v}$ and K represent the vector velocity and diffusivity, respectively, and S_c indicates the source-

131 minus-sink terms of the state variable C calculated at each grid. TOPAZ considers eight types of

132 biogeochemical processes: the dissolved organic matter (DOM) cycle, particle sinking, dry/wet

133 atmospheric decomposition, gas exchange, river input, removal, sediment input and scavenging (Dunne

134 et al., 2005; 2007). Various equations for these processes are available, utilizing relationships between

135 variables derived from observational data (Dunne et al., 2012). In addition, TOPAZ includes an "optical

136 feedback" module that considers the chlorophyll photosynthesis. Optical feedback calculates the total

137 surface irradiance($I(z)$) as a function of the solar radiation wavelength (Manizza et al., 2005). This

138 scheme regulates vertically penetrating irradiance due to shortwave radiation absorption in the visible

139 light, which is influenced by the distribution of chlorophyll concentration in the water column of the

140 model.

141 $$I(z) = I_{IR} \cdot e^{-k_{IR}^2} + I_{RED(z-1)} \cdot e^{-k_{(r)}\Delta z} + I_{BLUE(z-1)} \cdot e^{-k_{(b)}\Delta z}, \qquad (2)$$

142

143 where the first term in the right hand side represents the penetration of the infrared wavelength band,

144 and the second and third terms represent the photosynthetically active radiation (PAR), which is divided

145 into two visible wavelength bands, namely the red and blue/green bands. PAR is used to calculate the

146 growth rate of phytoplankton groups and is a key factor in biogeochemistry. For more detailed
147 information on TOPAZ, we refer to Dunne et al. (2012).

2.3 The coupled ROMS–TOPAZ model (NPRT version 1.0)

149   In this study, to couple ROMS with TOPAZ, we employed the stand-alone version of TOPAZ, which
150 was separated from the Modular Ocean Model version 5 (MOM5) developed by the GFDL in a previous
151 study (Jung et al., 2020). In this study for the stand-alone version of TOPAZ, the air–sea gas exchange
152 for CO_2 and O_2 is based on Wanninkhof (1992) and Najjar and Orr (1998), and the optical feedback is
153 based on Manniza et al. (2005). Furthermore, TOPAZ prescribes the surface flux from the atmosphere
154 to the ocean for nitrate (NO_3), ammonia (NH_4), lithogenic aluminosilicate (LITH), and dissolved iron
155 (Fed) (Jung et al., 2020). For these atmospheric chemistry values for the surface flux, this study employs
156 climatological monthly mean data as provided by the official MOM GitHub (https://mom-
157 ocean.github.io/docs/quick-start-guide/, last access: 1 March 2023).

158   Fig. 1 shows the structure of the NPRT. During the initialization process, TOPAZ receives the grid
159 and domain information from ROMS. Subsequently, integration with the *ROMS Main Driver* occurs to
160 calculate S_c within the "time step loop" using Eq. (1). Simultaneously, the chlorophyll optical feedback
161 is also considered in each time step, with the PAR modified by chlorophyll concentrations influencing
162 S_c, whereas the total radiation is used in the physical processes of ROMS. In the *ROMS Main Driver*,
163 the advection and diffusivity terms are calculated considering river runoff (Alk, DIC, NH_4, NO_3, LITH,
164 and PO_4). Information such as prognostic tracers, ocean physical variables, atmospheric forcing, and
165 dry/wet deposition (LITH, NH_4, NO_3, and Fed) are then transmitted to the TOPAZ module, where the
166 source/sink term (S_c) is calculated. In other words, the state variable *C* is calculated using data related
167 to the transport tendency of the tracers and source/sink term through the *ROMS physics* and
168 *generic_TOPAZ_column_physics* modules (Fig. 1).

2.4 Experimental setup

170   To operate NPRT, it is necessary to obtain the initial and boundary conditions for the
171 biogeochemical variables considered by TOPAZ; however, it is impossible to encompass all
172 biogeochemical observational data, since TOPAZ considers 30 prognostic and 11 diagnostic tracers.
173 Therefore, in this study, the results of MOM5–TOPAZ were employed as the initial and boundary
174 conditions of TOPAZ. To operate MOM5–TOPAZ, the default input datasets provided by the official
175 MOM GitHub were employed for the initial condition. MOM5–TOPAZ was initially operated for a 100-
176 year spin-up integration under a pCO_2 environment (369.6 ppm) and ECMWF Reanalysis v5 (ERA5;
177 Hersbach et al. 2020) of year 2000. Séférian et al. (2016) suggested that biochemical models require

178   spin-up times longer than those required by physical ocean models. However, in this study, we adopted

179   a 100-year spin-up time integration because of limited computing and time resources. After the 100-

180   year spin-up time integration, using the results from the last time step as the initial condition, MOM5–

181   TOPAZ was operated for 2000–2014, with a realistic atmospheric CO_2 concentration and atmospheric

182   forcings from ERA5. Through these spin-up process described above, the initial and boundary

183   conditions for the biogeochemical variables required to conduct NPRT were obtained. Nutrient

184   concentrations for dry/wet atmospheric deposition and runoff were obtained from the default input data

185   of the official MOM GitHub.

186   The initial and boundary conditions used for the physical variables were monthly mean data from

187   the Hybrid Coordinate Ocean Model (HYCOM) reanalysis with a 1/12° (approximately 8 km)

188   horizontal resolution. We used the six-hourly atmospheric external forcings, as provided by ERA5 as

189   well as climatological monthly mean discharges of 12 major rivers, including the Yangtze, Huanghe,

190   Yungsan, Keum, Han, Haihe, Luanhe, Amnokgang, Taedong, Qiantang, Pearl Rivers (Fig. 2; Kwon

191   2007). In addition, to obtain the tidal mixing effect, we considered 10 major tidal and tidal current

192   harmonic components (M_2, S_2, N_2, K_2, K_1, O_1, P_1, Q_1, M_f, and M_m) from TPX07 (Egbert and Erofeeva,

193   2002). The GLS vertical mixing scheme was used for parameterization (Umlauf and Burchard, 2003).

194   The bottom stress is parameterized with a quadratic drag law using a drag coefficient (2.5×10^{-3}), and

195   horizontal viscosity and diffusion coefficients are 25 m^2 s^{-1} and 50 m^2 s^{-1}, respectively.

196   In this study, the model domain (105–170° E, 13–52° N) is the Northwest Pacific (NWP), which is

197   one of the key regions for conducting global air–sea gas exchange, and includes the East/Japan Sea

198   (hereafter East Sea), the Yellow and East China Seas (YECS), and South China Sea (Fig. 2). The

199   horizontal resolution is 1/12°, both in longitude and latitude and the number of vertical layers is 50. The

200   bottom topography from GEBCO data (Weatherall et al. 2015) is interpolated onto the model grid.

201   NPRT was operated for a total of 15 years (2000–2014). To address the requirement for a sufficiently

202   long spin-up time for executing the biogeochemical model, we conducted an additional spin-up for the

203   initial five years. Therefore, in this study, the model results averaged over the last 10 years were used

204   for the analysis.

205   To compare NPRT simulations with available observational data, this study divided the Northwest

206   Pacific into four regions on the base of physical and biological environments: the NWP, further

207   subdivided into the subtropical (south of 40° N) and subarctic regions (north of 40° N), East Sea, and

208   YECS (Fig. 2). The SSH distribution was obtained from the Copernicus Marine Environment

209   Monitoring Service (CMEMS) satellite data from 2005 to 2014. Sea water temperature and salinity are

210   not only key factors in phytoplankton growth but also essential physical factors that determine the water

211 mass distribution in the ocean. In this study, the water temperature and salinity simulated from NPRT
212 were verified via annual and monthly climatological datasets from the World Ocean Atlas 2018
213 (WOA18) at a horizontal resolution of $1° \times 1°$. In addition, to evaluate the reproducibility of chlorophyll
214 concentrations, the Moderate Resolution Imaging Spectroradiometer (MODIS) and the Coupled Model
215 Intercomparison Project phase 6 (CMIP6; Eyring et al. 2016) were employed. As shown in Table1, this
216 study adopted six models from CMIP6, providing chlorophyll concentrations for the historical period
217 (2005–2014). Each model is a single ensemble member, typically the 'r1i1p1f1': r, i, p, and f denote the
218 realization, initialization, physics, and forcing indices, respectively (Taylor et al. 2018). For dissolved
219 oxygen and nutrients, we also used the annual and monthly climatological datasets from WOA18. In
220 addition, we utilized the conductivity–temperature–depth (CTD) measurement data such as DO, from
221 the Japan Meteorological Agency (JMA) along the 137° E line from 2005 to 2014. The simulated DIC
222 in NPRT was compared with observational data from the Global Ocean Data Analysis Project version
223 2 (GLODAPv2; Lauvset et al., 2016) with a horizontal resolution of $1° \times 1°$ and 33 vertical layers from
224 0 to 5,500 m. GLODAPv2 is the mapped climatology fields averaged from 1972 to 2013 at the Carbon
225 Dioxide Information Analysis Center (CDIAC).

226

3. Results and discussion

3.1. Physics

229 The study area is characterized by diverse oceanic environments, which determine the
230 biogeochemical characteristics. For example, in the Kuroshio–Oyashio Confluence Region, the
231 distributions of biogeochemical variables are determined by various physical and biological processes,
232 such as advection, horizontal mixing, vertical mixing, photosynthesis, and respiration. In addition, the
233 YECS is a river-dominated marginal sea, where large amounts of nutrients are discharged into the sea
234 along with freshwater (Dai et al., 2022; Na et al., 2024). Therefore, to accurately simulate the
235 biogeochemical properties, validating the oceanic physical characteristics, such as water temperature,
236 current, and salinity, is necessary. The distribution of ocean currents, in conjunction with water
237 temperature and salinity, is essential for determining the oceanic physical characteristics. This key factor
238 plays a fundamental role in direct and indirect assessments of all aspects of the marine environment. To
239 validate the reproducibility of the physical characteristics, the simulated SSH data were compared with
240 satellite-observed altimetry data from CMEMS.

241 Fig. 3 shows the long-term mean SSH distributions in CMEMS and NPRT during 2005–2014. The
242 Kuroshio Current originates from east of the Philippine coast, where it flows northeastward, passes

through the Tokara Strait, and continues eastward, meandering along the southern coast of Japan. Furthermore, in the Shikoku Basin, there is a long-standing anticyclonic eddy associated with ocean-bottom topography (Ding et al., 2022). In the subarctic region, the Oyashio Current flows southward and converges with the Kuroshio Current, resulting in the mixing of distinct water masses; the region where this happens is known as Kuroshio–Oyashio Confluence Region (Sugimoto and Hanawa, 2011; Zhu et al., 2019). As mentioned previously, the NPRT results generally agree well with the observed characteristics of the upper-layer circulation system in the NWP.

Fig. 4 shows the annual mean sea surface temperature (SST) in WOA18 and NPRT. The Northwest Pacific exhibits subtropical characteristics, with high temperatures above 25 °C approximately 20° N. Additionally, this region is predominantly influenced by the Kuroshio Current with warm water mass, which results in the northward distribution of isotherms along the Japanese coast. As mentioned above, a significant north–south temperature gradient is also observed between 35° N and 40° N, corresponding to the Kuroshio–Oyashio Confluence Region. The characteristics of the SST distribution in the Northwest Pacific are highly pronounced in NPRT, although the simulated sea surface temperature predominantly shows a positive bias, with a particularly significant positive bias (> 4°C) observed in the Kuroshio–Oyashio Confluence Region (Fig. 4c). Notably, the location of the Kuroshio–Oyashio Confluence Region, which plays a crucial role in the formation of the North Pacific Intermediate Water (NPIW), is also accurately simulated.

The NPIW is characterized by salinity and potential vorticity minima, with its primarily distributed between density 26.6 and 27.2 σ_θ, corresponding to depths of 600–800 m (Lembke-Jene et al., 2017). The NPIW transports large amounts of nutrients to the NWP. Therefore, simulating the NPIW is important for the reproduction of biogeochemical characteristics in the NWP. Comparing the vertical structures of zonal mean salinity between 140° and 160° E to those in the WOA18 data shows that the depth of the salinity minimum layer is approximately 600–800 m, similar to the observational data (Fig. 5). However, the salinity minimum layer is about 0.2 psu higher than that of the observations. This is attributed to a significant positive bias of salinity simulated in NPRT in Kuroshio–Oyashio Confluence Region. Nevertheless, NPRT adequately reproduces not only the surface currents but also the ventilation for the formation of the NPIW.

The YECS are characterized by the dominant effects of tidal mixing and runoff. Freshwater discharged from the Yangtze River, one of the major sources of nutrients in the East China Sea, forms a low-salinity plume that spreads and influences the stratifications of the surrounding areas (Moon et al., 2009). NPRT did not include all rivers in the YECS; nevertheless, a total of 12 rivers, including the Yangtze River, were included (Fig. 2). Regarding the oceanographic characteristics of the YECS, the

model exhibits similar patterns with those of the observations from WOA18, despite of a negative bias (Fig. 6 and Supplement Fig. 1). During winter (February; Fig. 6e and Supplement Fig. 1e), the simulated sea surface salinity distribution in the YECS is below 32.0 psu, whereas during the freshwater discharge-intensive summer (August; Fig. 6f and Supplement Fig. 1f), the salinity drops below 30 psu, forming a low-salinity tongue shaped feature extending toward the Korean coast. In the NWP, high salinity water (> 34.0 psu) extends northward to around 40° N during winter and around 35° N during summer. The reproduced distinct seasonal variability is similar to that in the WOA18 data, with all spatial correlation coefficients and root-mean-square error (RMSE) for surface salinity distribution in the annual mean, winter, and summer being over 0.93 and 0.33–0.42 psu, respectively.

Overall, NPRT reasonably simulates the major characteristics observed in each region and is, therefore, suitable for analyzing the spatiotemporal distribution and characteristics of chlorophyll concentration, nutrients, and the carbon cycle influenced by these physical properties.

3.2. Biogeochemistry

3.2.1 Nutrients

The results of the simulated nitrates, phosphates, and silicates, which are essential for the growth of phytoplankton, were compared with the results of the observationally base WOA18 climatology (Figs. 7–9). Fig. 7a–c shows the comparison of the simulated surface annual mean nitrates with the observed ones. The distribution of the annual mean surface nitrate concentration in the observational data reveals a characteristic increase from low to high latitudes, with concentrations exceeding 15 μmol kg^{-1} in the subarctic region (Fig. 7a). In the model results, the annual mean concentration of nitrate also increases with increasing latitude and is predominantly distributed in the East Sea, Okhotsk Sea, and the Oyashio extension region (Fig. 7b). Compared with that in the observations, the overall distribution of annual mean surface nitrate concentrations is underestimated (Fig. 7c). In particular, in the subarctic region, the model results exhibit a large negative bias of over -10 μmol kg^{-1}, whereas in the East Sea and the Kuroshio and its extension regions, it exhibits a positive bias. The pattern correlation and RMSE for nitrate in the study area are 0.83 and 5.70 μmol kg^{-1}, respectively. The distribution of the annual mean surface phosphates in NPRT is similar to that in WOA18 (pattern correlation: 0.83; Fig. 8a, b). However, there is a negative bias in the subarctic region and a positive bias in the eastern coast of Sakhalin and the East Sea (Fig. 8c). The bias range is approximately -1.2–0.5, and the RMSE is approximately 0.53 μmol kg^{-1}. Unlike other nutrients, the simulated silicate exhibits a significant positive bias (> 30 μmol kg^{-1}) and a negative bias (> 30 μmol kg^{-1}) in the YECS and the subarctic region, respectively (Fig. 9c).

308 The TOPAZ module is suitable for analyzing the biogeochemical environment in the ocean; however,
309 the reproducibility of its results in marginal seas, such as the YECS, where riverine and tidal effects are
310 important, might be limited. Therefore, for accurate reproduction, it is necessary to adjust various
311 parameters based on precise river discharge data.

312 The vertical errors of the zonally averaged annual mean nutrients (nitrate, phosphate, and silicate) in
313 the NWP were overestimated south of the Kuroshio–Oyashio Confluence Region (40° N) until a depth
314 of 500 m (Fig. 10). However, in the 500–1500 m, the underestimation error in the 500–1500 m appears,
315 which seems to be related to the NPIW simulation. In the intermediate layer of the NWP, the subarctic
316 intermediate water nutrient pool (SINP) with high nutrient concentrations appears along with the NPIW
317 formed in the Kuroshio–Oyashio Confluence Region (Nishioka et al., 2020; 2021). However, it is
318 considered that the SINP is not distinct in NPRT due to the negative bias in the subarctic region, which
319 is the source of the SINP. Positive biases for nutrients were distributed within a depth of 500 m in all
320 seasons, similar to the annual mean bias, while negative biases exhibited in deeper depths (black solid
321 line in Fig. 10c, f, i). Regardless of the season, the depth of the positive bias peak for all nutrients is
322 approximately 100–300 m.

323 The simulated surface nutrient concentrations in NPRT exhibited a clear seasonal variability (Figs.
324 7–9). In winter, high nitrate concentrations distributed in the subsurface are supplied to the surface by
325 vertical mixing, resulting in an increase in the upper–layer nutrient concentrations from winter to spring.
326 In summer and autumn, distinct seasonal variability is observed, with concentrations gradually
327 decreasing owing to enhanced stratification. The temporal correlation coefficients between model
328 results and observations (WOA18) for nutrients (nitrate, phosphate, and silicate) are approximately
329 0.78–0.98, indicating that the seasonal variability is well represented, except for the silicate
330 concentration in the YECS (temporal correlation coefficient: 0.47). In the subarctic region, all nutrients
331 are consistently underestimated regardless of the season, which is likely attributed to the initial and
332 boundary biogeochemical conditions. The initial conditions for nutrients derived from the MOM5–
333 TOPAZ results are approximately 10 $\mu mol\ kg^{-1}$ lower than those derived from the WOA18 data (not
334 shown here).

335 In addition, we need to pay particular attention to the overestimation of silicate in the YECS (Fig. 9).
336 In TOPAZ, silicate is regulated through biogeochemical processes such as dissolution and uptake by
337 large phytoplankton within the mixed layer, as well as particles sinking into the deep ocean (Dunne et
338 al. 2012). In NPRT, the overestimation of the silicate concentration can be attributed to two possible
339 factors. The first possibility is that silicate, unlike other nutrients, is only considered taken up by large
340 phytoplankton. The second factor is that the YECS, which is a shallow marginal sea with a maximum

depth of less than 50 m, experiences strong vertical mixing throughout the entire water column due to strong winds, surface heat fluxes during winter, and tidal effects. In shallow marginal seas, rather than a decrease in the upper layer silicate concentration due to particles sinking into the deep ocean, it is speculated that particles remain within the mixed layer, continuously increasing through dissolution. To address the large bias in silicates observed in marginal seas such as the YECS, it is necessary to consider the specific marine environment of each region and adopt accurate parameters and external forcings.

To statistically evaluate the reproducibility of NPRT, this study calculated the monthly Taylor diagram score (TD score; Taylor, 2001; Jin et al. 2023) in each region (Table 1) via the following formulation.

$$TD(Taylor\ diagram)\ Score = \ |1 - R| + \left|1 - \frac{\sigma_M}{\sigma_O}\right| + \frac{E'}{\sigma_O}\ , \qquad (3)$$

where R is the pattern correlation, and where σ_M and σ_O indicate the standard deviations in the model and observations, respectively. E' is the RMSE. The TD scores for nitrate and phosphate concentrations tend to increase from summer to winter, except in the Subarctic region. In particular, the TD scores for nitrate in the subtropical region sharply increase in November and December (Table 1), which is due to the large bias distribution in the Kuroshio–Oyashio Confluence Region (not shown here). The positive bias distributed in this region is thought to be due to the relatively high nutrient concentrations in the subsurface in NPRT, which are transported to the surface layer through vertical mixing (Fig. 10). In the Subarctic region, the TD scores for all nutrients are greater than 2.5 (Table 1), but as mentioned above, the seasonal variability is well reproduced. Therefore, the dominant negative bias is expected to improve significantly with the use of more accurate initial and boundary conditions. The TD scores for nitrate and phosphate in the East Sea and the YECS are approximately 1.0–2.5 higher than those in the subtropical region. In the case of silicate, the TD score is greater than 10.0 for all months.

3.2.2 N:P ratio

The study area, the Northwestern Pacific, can be broadly divided into three limitation regions: the subtropical and subarctic regions and the YECS, which are characterized by nitrogen limitation (Browing et al. 2022), Fe limitation (Watson, 2001; Zhang et al 2021), and phosphate limitation (Lee et al. 2023), respectively. The N:P molar ratio in seawater is commonly used to evaluate whether the growth of phytoplankton is potentially limited by nitrogen or phosphorus. Fig. 11 shows the distribution pattern of the N:P molar ratio in the Northwestern Pacific. In the subtropical region, the N:P ratio in WOA18 and NPRT were approximately 3.4 and 4.3, respectively. However, NPRT shows a clear

373 positive bias in the Kuroshio Current and its extension region. This characteristic is also evident in the

374 distribution of nutrient biases (Fig. 11c). The large meander of the Kuroshio Western Boundary Current

375 significantly influences not only physical characteristics but also biological processes (Hayashida et al.

376 2023). Therefore, to accurately analyze the biological processes in the Kuroshio meandering region in the

377 future, it is important to consider improving the model's representation of Kuroshio meandering. In

378 WOA18, the N:P molar ratio in the YECS was approximately 7.3, with the ratio exceeding 16.0,

379 particularly at the Yangtze River estuary, where a distinct phosphate limitation region is observed (Fig.

380 11a). However, the simulated N:P ratio was relatively lower than the observed values in the Yangtze

381 River estuary (Fig. 11b). As mentioned earlier, despite the significant influence of river discharge in

382 regions such as the YECS, the relatively low N:P molar ratio simulated in this study is likely due to

383 inaccuracies in the estimated nutrient input from riverine sources.

384

3.2.3 Chlorophyll

386 The characteristics of the simulated chlorophyll distributions were compared with those inferred

387 from MODIS satellite data (Fig. 12). The chlorophyll concentrations derived from satellite data include

388 both sea surface and mixed layer components due to the backscattering effect of reflected light (Park et

389 al., 2014; Jochum et al., 2019; Jung et al., 2020). Therefore, in this study, 0–20 m depth-averaged

390 chlorophyll concentrations from NPRT were compared with satellite data for 2005–2014. In addition,

391 we analyzed the characteristics of the high-resolution regional model (NPRT) compared with the global

392 biogeochemical models in the CMIP6 datasets. Biogeochemical models include various variables,

393 among which the chlorophyll concentration is influenced by physical factors (temperature and

394 circulation system), light, and various nutrients, and it exhibits distinct seasonal variability. In this study,

395 we considered it a representative variable for evaluating the performance of biogeochemical models

396 and used a total of 13 ensemble members in the CMIP6 models (Table 2). Among the 13 members

397 (Table 2), ensemble numbers 1 to 8 were calculated using the 0–20 m depth averaged chlorophyll

398 concentration, whereas the remaining ensembles provided only surface data. In addition, we compared

399 the chlorophyll concentration of GFDL–ESM2M and GFDL–ESM2G (hereafter ESM2M and ESM2G),

400 which published in IPCC AR 5, with the NPRT results. Since the historical data for ESM2M and

401 ESM2G are available only up to 2005, we analyzed the data from 1996 to 2005.

402 Since the chlorophyll distribution and seasonal variation exhibit different characteristics in each

403 region, the analysis in this study was divided into subtropical and subarctic regions, the East Sea, and

404 the YECS. First, when the data from subtropical and subarctic regions and the East Sea are analyzed,

405 the chlorophyll concentrations generally increase from low to high latitudes according to observations

(Fig. 12a). In NPRT, the distribution of the annual mean chlorophyll concentration was similar to the observations in the subtropical region and the East Sea (pattern correlations: 0.72 and 0.61, respectively). However, a positive bias is dominant regardless of season, primarily due to the positive bias in nutrients related to phytoplankton growth (Figs. 7–9). Despite the positive biases in the chlorophyll concentration distributions in the subtropical and subarctic regions and the East Sea, as represented in NPRT, the seasonal variation in the chlorophyll concentration, which has spring and autumn biomass peaks), was similar to the observations (Fig. 13a, b, c). The reproducibility of seasonal variability in NPRT is comparable to the results of ESM2M and ESM2G. However, most of the results of the CMIP6 models do not adequately capture the autumn peak in the subtropical and subarctic regions and East Sea. The pattern correlation ranges of the annual mean chlorophyll concentrations for each ensemble member of CMIP6 in the subtropical and subarctic regions and the East Sea are -0.06–0.61, -0.39–0.65 and -0.15–0.17, respectively (Fig. 14). Some models in the CMIP6 datasets show negative pattern correlations. Although ESM2M and ESM2G showed a good representation, the range of pattern correlation coefficients was quite low, ranging from -0.12–0.26. As a result, the TD scores in NPRT are lower than those in the ESM2M, ESM2G, and CMIP6, especially in the East Sea, and the reproducibility of the chlorophyll concentration distribution has significantly improved (Table 3).

In the YECS, the spatial correlation coefficient in NPRT was approximately 0.45 (Fig. 12a, b and 14d), a relatively low value compared to other regions. However, NPRT simulated biomass blooms near the Yangtze River and along the Chinese coast, driven by high freshwater discharge (Fig. 12b). In addition, NPRT, ESM2M and ESM2G effectively reproduced the seasonal variability (spring peak and increasing from summer) that was not captured by CMIP6 models. In the case of the CMIP6 models, negative bias is dominant regardless of the season (Fig. 13d), and they also lack clear seasonal variability in the chlorophyll concentration. In the YECS, the discharge of freshwater and nutrient concentrations from rivers is one of the most important input forcings determining the spatiotemporal pattern and variability (Zhou et al., 2008). In this study, to apply observation data for freshwater discharge and nutrient concentrations from river outflows, tracer concentrations were determined with a volume flux at the river source point, following an approach similar to that adopted in regional biogeochemical models such as FENNEL (Fennel et al. 2006) and a modified version of the Carbon, Ocean, Biogeochemistry and Lower Trophic (COBALT; Hauri et al. 2020). However, the chlorophyll concentrations in NPRT still tend to be underestimated (RMSE: 1.62 μmol kg^{-1}) in the YECS, including the Yangtze River estuary (Fig. 12c). Nonetheless, the TD score in NPRT was approximately 2.32, which is lower than that in the ESM2M, ESM2G, and CMIP6 (2.23–3.5) (Table 3), and NPRT reproduced the seasonal variability (Fig. 13d) and spatial characteristics such as biomass blooms near the Yangtze River and along the Chinese coast, driven by high freshwater discharge (Fig. 12b).

440   In the YECS, the underestimated chlorophyll concentration in NPRT may also be related to the
441 distribution of low nutrient concentrations in the YECS. Furthermore, this can be attributed to the
442 incomplete consideration of the influences exerted by numerous rivers along the Chinese and Korean
443 coasts as well as the utilization of default data provided by MOM GitHub, which deviates from the
444 actual diverse biogeochemical variables (LITH, NH_4, NO_3, and Fed) introduced from the atmosphere.
445 In addition, we need to consider the uncertainties associated with the satellite observational data from
446 MODIS. MODIS indirectly estimates chlorophyll concentrations by measuring the spectrum of light
447 reflected from the sea surface (visible and near-infrared); however, completely eliminating the influence
448 of colored dissolved organic matter (CDOM) and suspended particles in the water is difficult. Coastal
449 regions, classified as type II waters, are particularly prone to bias in estimated surface chlorophyll
450 concentrations due to the high concentrations of CDOM and suspended particles (Mauri et al. 2007).
451 The CDOM calculated using MODIS data was significantly greater in the YECS than in the other
452 regions (Supplement Fig. 2), and the absorption of blue light by CDOM can lead to an overestimation
453 of the chlorophyll concentration (Fig. 12 and Supplement Fig. 2). In other words, owing to the influence
454 of CDOM, the chlorophyll distribution observed by MODIS may be overestimated, potentially leading
455 to a negative bias in the chlorophyll simulated by NPRT in the YECS. Furthermore, CDOM enhances
456 shortwave heating at the surface while reducing it below the surface (Kim et al. 2016). This process
457 can influence penetrating shortwave radiation, mixing, and surface heat flux. Focusing on the
458 variability in physical processes caused by CDOM could greatly contribute to future research on
459 the interactions between biogeochemistry and physical oceanography.

460

461   **3.2.4 Dissolved inorganic carbon and alkalinity**

462   The variables of the carbon system, including dissolved inorganic carbonic (DIC) and alkalinity
463 (Alk), simulated in NPRT were analyzed. First, DIC is a crucial component of ocean biogeochemistry
464 and is directly linked to plankton photosynthesis and respiration; hence, it is a valuable parameter for
465 the analysis of the carbon system (Ding et al., 2018). The results of NPRT, averaged from 2005 to 2014,
466 were compared with the observed climatological data obtained from GLODAPv2 (Fig. 15a–c). For both
467 the model results and observational data, the annual mean surface DIC concentration in the subarctic
468 region is significantly higher than that in the subtropical region. The simulated annual mean surface
469 DIC concentration in NPRT generally exhibited a positive bias. However, in the YECS, there was a
470 significant negative bias of over -300 µmol kg^{-1}. In particular, low DIC concentrations (below 1,900
471 µmol kg^{-1}) appeared in the Yangtze River estuary. The bias range for the entire study area is
472 approximately between -650 and 180 µmol kg^{-1}, with a pattern correlation of approximately 0.41 and a

473   RMSE of 99.84 µmol kg^{-1}, respectively. The GLODAPv2 dataset does not seem to adequately reproduce

474   the low DIC concentrations caused by the discharge from the Yangtze River. This is because previous

475   studies using ship-based observations have reported that the low concentration are distinctly observed

476   in the Yangtze River estuary (Zhai et al., 2007; Wang et al., 2016). If the YECS are not considered,

477   the pattern correlation and RMSE excluding the YECS are approximately 0.81 and 95.67 µmol kg^{-1}.

478   The alkalinity (Alk) simulated in NPRT also exhibited a significant positive bias (> 400 µmol kg^{-1})

479   in the study area, excluding the YECS (Fig. 15d–f). Overestimated Alk in NPRT facilitates the

480   accumulation of pCO$_2$ from the atmosphere into the ocean, which may contribute to the increase in

481   surface DIC concentration. The simulated annual mean surface CO$_2$ flux was predominantly

482   characterized by an influx from the atmosphere to the ocean (Fig. 16). However, it may be premature

483   to conclude that the results of carbonate variables in NPRT are positively biased because time series of

484   DIC concentration in MOM5–TOPAZ did not reach equilibrium state during the spin-up period

485   (Supplement Fig. 3). Consequently, the initial and boundary conditions derived from the MOM5–

486   TOPAZ model results exhibit significantly higher DIC concentrations and Alk than the observations. In

487   particular, the DIC concentration at the eastern boundary is higher than that observed, which may

488   contribute to the elevated DIC levels in the subtropical region due to the influence of North Equatorial

489   Current and Kuroshio Current. To improve this bias, more accurate boundary conditions must be

490   considered.

491

3.2.5 Dissolved Oxygen

493   DO is important for analyzing the ecological and physical characteristics of marine

494   ecosystems and serves as a tracer. It is associated with ocean temperature, air–sea exchange,

495   and phytoplankton photosynthesis. The simulated DO results were compared with the WOA18

496   climatological data and observations from the JMA (Figs. 17 and 18). Both the observations (i.e.,

497   WOA18) and the model results demonstrate a typical increase in surface DO concentrations from low

498   to high latitudes, with high concentrations of DO more than 300 µmol kg^{-1} being distributed in the

499   Okhotsk Sea and the Oyashio region (Fig. 17). With respect to that of the WOA18 observations, the

500   model tends to underestimate DO exhibiting a dominant negative bias (up to approximately -30 µmol

501   kg^{-1}) in the Oyashio region. The pattern correlation and the RMSE of DO concentration between the

502   model results and WOA18 data are 0.99 and 9.99 µmol kg^{-1}, respectively. The primary cause of the

503   negative bias in the simulated DO is related to the positive bias in surface temperature (Fig. 4c and 17c),

504   which is thought to be due to the weakening of thermal solubility. To compare the vertical structures of

505   DO, ship measured DO data from the JMA were employed along the 137° E line across the Kuroshio

506   main path in January and June (Fig. 18). Both the observations and the model results show the presence

507   of an oxycline layer, where the DO decreases sharply with depth. Below this layer, DO minimum zone

508   is evident. However, the depth of the DO minimum zone in NPRT appears below 500 m regardless of

509   the season, similar to the observations (JMA); however, the minimum DO concentrations are

510   approximately 25 µmol kg^{-1} higher than the JMA data. This is presumed to be caused by the weak NPIW

511   formation. These characteristics are also evident in the results obtained using the TOPAZ module (Lee

512   et al., 2022). Consequently, NPRT adequately qualitatively reproduces the spatiotemporal distribution

513   of the DO circulation system. However, sufficient observational data, accurate initial and boundary

514   conditions, improvement in physical processes simulation, and adequate spin-up times are required for

515   quantitative and reproducibility improvements, particularly in the intermediate layer.

516

4. Conclusions

518   The coupled physical–biogeochemical ocean model developed in this study, namely ROMS–TOPAZ

519   (NPRT v1.0), is a preliminary investigation that reflects the characteristics of local regions with high

520   resolution, enabling analysis of the interactions between the physical and biogeochemical processes in

521   the ocean. The study area comprises the NWP, East Sea and YECS, which exhibit diverse characteristics

522   depending on the region. The study area is one of the main regions where nutrients are consumed by

523   primary production. CO_2 exchange between the air and sea is dominant in the NWP (Takahashi et al.,

524   2009; Ishizu et al., 2021); however, in the YECS, the biogeochemical environment is significantly

525   influenced by riverine discharge (Zhou et al., 2008). In these oceanic regions with such diverse features,

526   we evaluated the reproducibility of the spatial distribution and seasonal variability of the physical and

527   biogeochemical variables derived using NPRT. To generate the initial and boundary data for the

528   biogeochemical variables required to simulate NPRT, first, MOM5–TOPAZ was integrated for 100

529   years under the pCO_2 environment, and ERA5 was integrated for 2000, after which it was conducted

530   for an additional 15 years under actual atmospheric CO_2 concentration conditions (2000–2014). Using

531   the biogeochemical variables reproduced by MOM5–TOPAZ and the physical variables from HYCOM,

532   NPRT was subsequently integrated for 15 years (2000–2014). In this study, model results from the last

533   10 years (2005–2014) were used in the analysis.

534   NPRT successfully reproduced the overall spatial distributions, such as upper-layer circulation, the

535   NPIW formation via ventilation, and salinity in the YECS influenced by freshwater input, as well as the

536   seasonal variability in biogeochemical variables. For nutrients (nitrate, phosphates, and silicate), there

537   was a high pattern correlation coefficient for the annual mean surface nutrient concentrations. In

538   particular, both pattern correlations coefficient for nitrate and phosphate concentrations in the study

area are approximately 0.83, but the coefficient for silicate is low (approximately 0.42). All nutrients were underestimated in the subarctic region regardless of season, likely because low values were prescribed for the initial and boundary conditions. In contrast, the Kuroshio–Oyashio Confluence Region, characterized by strong vertical mixing, exhibited a positive bias, especially during winter, due to the relatively high nutrient concentrations at the subsurface in NPRT. Although biases are distributed depending on the region, the overall seasonal variability in all nutrients is well simulated. The temporal correlation coefficients for nutrients are approximately 0.78–0.98 in the study area, except for the silicate content in the YECS. In marginal seas at shallow depths, such as the YECS, silicate is presumed to accumulate continuously because of insufficient reduction caused by phytoplankton uptake and particles sinking into the deep ocean, leading to a significant positive bias. In other words, parameter adjustments considering physical and biogeochemical environments are necessary.

For chlorophyll concentration, although NPRT showed positive and negative biases in the study area, it effectively reproduced not only the seasonal variation in the subtropical and subarctic regions, East Sea, and YCES, but also the improved TD scores in all regions compared with the ESM2M, ESM2G, and CMIP6 data. In addition, in the YECS, because a significant amount of nutrients is discharged from the Yangtze River along with a large amount of freshwater, leading to biomass blooms around the Yangtze River estuary, the chlorophyll concentrations start to increase from July. As a result, low DIC concentrations associated with river effects were also simulated around the Yangtze River. These regional characteristics are difficult to reproduce via low-resolution global models. Furthermore, in the subtropical and subarctic regions, significant positive biases for DIC and Alk were predominantly simulated, which is due to the spin-up time (100 years) in this study being insufficient for reaching equilibrium state.

In summary, the coupled model NPRT developed in this study is an important tool for studying the interactions between ocean physics and biogeochemistry at a high resolution, enabling research at the regional scale. In the future, this tool is expected to provide a basis for understanding the mechanisms of oceanic physics and biogeochemical environments in various regions, ultimately improving the accurate assessment and predictability of carbon cycling.

571 *Acknowledgments.*

572   This work has been supported by Basic Science Research Program through the National Research Foundation

573 of Korea (NRF) funded by the Ministry of Education (RS-2024-00451970 and RS-2024-00461585), and the

574 National Research Foundation of Korea (NRF) grant funded by the Korea government (MIST) (NRF-

575 2022M3I6A1086449). The main calculations were performed by using the supercomputing resource of

576 the Korea Meteorological Administration (National Center for Meteorological Supercomputer).

577

578 *Code Availability.*

579   ROMS–TOPAZ   (NPRT   v1.0)   used   in   this   study   is   archived   on   Zenodo

580 (https://doi.org/10.5281/zenodo.11218350). In addition, the input data (initial, boundary, atmospheric

581 forcings, atmospheric deposition data) for conducting NPRT and the model results are archived on

582 Zenodo (https://zenodo.org/records/13941078).

583

584 *Data availability statement.*

585   The data analyzed in this study are available from public websites. Bathymetric data were

586 provided by GEBCO (GEBCO Compilation Group, 2021; GEBCO_2021 Grid,

587 https://doi.org/10.5285/c6612cbe-50b3-0cffe053-6c86abc09f8f, GEBCO, 2022, last access: 1 March

588 2023). The atmospheric forcings were provided by ECMWF Reanalysis v5 (ERA5;

589 https://cds.climate.copernicus.eu/cdsapp#!/search?type=dataset:1 March 2023). For conducting the

590 MOM–TOPAZ model, the input data for initial, boundary, and dry/wet atmospheric deposition were

591 provided by MOM GitHub (https://mom-ocean.github.io/docs/quick-start-guide/, last access: 1 March

592 2023). For conducting NPRT, the physical ocean initial and boundary data were used from Hybrid

593 Coordinate Ocean Model (HYCOM; https://tds.hycom.org/thredds/catalog.html:1 December 2023).

594 The SSH data were obtained from the Copernicus Marine and Environment Monitoring Service

595 (CMEMS; http://marine.copernicus.eu, last access: 15 November 2023). The data used to evaluate the

596 model results in this study are freely available online from Japan Meteorological Agency (JMA;

597 https://www.data.jma.go.jp/gmd/kaiyou/db/vessel_obs/data-report/html/ship/ship_e.php), World

598 Ocean Atlas 2018 (WOA18; https://www.ncei.noaa.gov/access/world-ocean-atlas-2018), , Moderate

599 Resolution Imaging Spectroradiometer (MODIS; http://www.daac.gsfc.nasa.gov/data/dataset/

600 MODIS/) for chlorophyll concentration, and GLODAPv2 (GLODPAv2;

601 (https://www.ncei.noaa.gov/access/ocean-carbon-acidification-data-system/

602 oceans/GLODAPv2_2022) for dissolved inorganic carbon. The CMIP6 model datasets are freely

603 available online (https://aims2.llnl.gov/search/cmip6, last access: 1 December 2023). Discharge data

604 for Yangtze River dataset are available online (https://www.cjh.com.cn/, last access: 24 September

605 2023). The colored dissolved organic matter (CDOM) is freely available online

606 (https://oceandata.sci.gsfc.nasa.gov/l3/, last access: 15 January 2025).

607

608 *Author Contribution.*

609 DK, HCJ, and JHM designed the study. DK and HCJ conducted the models and the simulations

610 and primarily responsible for developing ROMS–TOPAZ (NPRT v1.0). NHL analyzed CMIP6 data.

611 All authors analyzed and discussed the results and contributed to writing and editing of the article.

612

613 *Competing interests.*

614 The authors declare that they have no conflict of interest.

615

616

617

618

619

620

621

622

623

624

625

626

627

628

629

630

631

632

633

634

635

References

Arakawa, A. and Lamb, V. R.: Computational design of the basic dynamical processes of the UCLA general circulation model, in: General circulation models of the atmosphere, Meth. Comput. Phys., edited by: Chang, J., Elsevier, 17, 173–265, https://doi.org/10.1016/B978-0-12-460817-7.50009-4, 1977.

Browning, T. J., Liu, X., Zhang, R., Wen, Z., Liu, J., Zhou, Y., Xu, F., Cai, Y., Zhou, K., Cao, Z., Zhu, Y., Achterberg, E. P., and Dai, M.: Nutrient co-limitation in the subtropical Northwest Pacific, Limnol. Oceanogr. Lett., 7, 52–61, https://doi.org/10.1002/lol2.10205, 2022.

Chierici, M., Fransson, A., and Nojiri, Y.: Biogeochemical processes as drivers of surface fCO$_2$ in contrasting provinces in the subarctic North Pacific Ocean, Global Biogeochem. Cycles, 20, GB1009, https://doi.org/10.1029/2004GB002356, 2006.

Dai, M., Su, J., Zhao, Y., Hofmann, F. E., Cao, Z., Cai, W.-J., Gan, J., Lacroix, F., Laruelle, G. G., Meng, F., Müller, D., Regnier, P. A.G., Wang, G., and Wang, Z.: Carbon fluxes in the coastal ocean: synthesis, boundaty processes, and future trends, Annu. Rev. Earth Planet. Sci., 50, 593-626, https://doi.org/10.1146/annurev-earth-032320-090746, 2022.

Ding, L., Ge, T., Gao, H., Luo, C., Xue, Y., Druffel, E.R.M., and Wang, X.: Large variability of dissolved inorganic radiocarbon in the Kuroshio extension of the Northwest North Pacific, Radiocarbon, 60, 691–704, https://doi.org/10.1017/RDC.2017.143, 2018.

Ding, Y., Yu, F., Ren, Q., Nan, F., Wang, R., Liu, Y., and Tang, Y.: The physical-biogeochemical responses to a subsurface Anticyclonic eddy in the northwest Pacific. Front. Mar. Sci. 8. https://doi.org/10.3389/fmars.2021.766544, 2022.

Dunne, J. P., Armstrong, R. A., Gnanadesikan, A., and Sarmiento, J. L.: Empirical and mechanistic models for the particle export ratio, Global Biogeochem. Cycles, 19, GB4026, https://doi.org/10.1029/2004GB002390, 2005.

Dunne, J. P., Sarmiento, J. L., and Gnanadesikan, A.: A synthesis of global particle export from the surface ocean and cycling through the ocean interior and on the seafloor, Global Biogeochem. Cy., 21, GB4006, https://doi.org/10.1029/2006GB002907, 2007.

Dunne, J. P., John, J. G., Adcroft, A. J., Griffies, S. M., Hallberg, R. W., Shevliakova, E., Stouffer, R. J., Cooke, W., Dunne, K. A., Harrison, M. J., Krasting, J. P., Malyshev, S. L., Milly, P. C. D., Phillipps, P. J., Sentman, L. T., Samuels, B. L., Spelman, M. J., Winton, M., Wittenberg, A. T., and Zadeh, N.: GFDL's ESM2 Global Coupled Climate–Carbon Earth System Models. Part I: Physical Formulation and Baseline Simulation Characteristics, J. Climate, 25, 6646–6665, https://doi.org/10.1175/jcli-d11-00560.1, 2012.

Egbert, G. D. and Erofeeva, S. Y.: Efficient inverse modeling of barotropic ocean tides, J. Atmos. Ocean. Technol., 19, 183–204, https://doi.org/10.1175/1520-0426(2002)019<0183:EIMOBO>2.0.CO;2, 2002.

Eyring, V., Bony, S., Meehl, G. A., Senior, C. A., Stevens, B., Stouffer, R. J., and Taylor, K. E.: Overview of the Coupled Model Intercomparison Project Phase 6 (CMIP6) experimental design and organization, Geosci. Model Dev., 9, 1937–1958, https://doi.org/10.5194/gmd-9-1937-2016, 2016.

Fairall, C. W., Bradley, E. F., Rogers, D. P., Edson, J. B., and Young, G. S.: Bulk parameterization of air-sea fluxes for tropical oceanglobal atmosphere Coupled-Ocean Atmosphere Response Experiment, J. Geophys. Res., 101, 3747–3764, https://doi.org/10.1029/95JC03205, 1996.

Fennel, K, Wilkin, J., Levin, J., Moisan, J., O'Reilly, J., and Haidvogel, D.: Nitrogen cycling in the Middle Atlantic Bight: Results from a three-dimensional model and implications for the North Atlantic nitrogen budget, Global Biogeochemical Cycles, 20(3), 2005GB002456, https://doi.org/10.1029/2005GB002456, 2006.

Hanawa, K., and Mitsudera, H.: Variation of water system distribution in the Sanriku coastal area, J. Oceanogr. Soc. Jap., 42, 435-446, https://doi.org/10.1007/BF02110194, 1987.

681 Hauri, C., Schultz, C., Hedstrom, K., Danielson, S., Irving, B., Doney, S. C., Dussin, R., Curchitser, E. N., Hill,
682   D. F., and Stock, C. A.: A regional hindcast model simulating ecosystem dynamics, inorganic carbon
683   chemistry and ocean acidification in the Gulf of Alaska, Biogeosciences, 17, 3837-3857,
684   https://doi.org/10.5194/bg-17-3837-2020, 2020.

685 Hayashida, H., Kiss, A. E., Miyama, T., Miyazawa, Y., and Yasunaka, S.: Anomalous nutricline drives marked
686   biogeochemical contrasts during the Kuroshio Large Meander. J Geophys Res (Oceans) 128:e2023JC019697,
687   https://doi.org/10.1029/2023JC019697, 2023.

688 Hersbach, H., Bell, B., Berrisford, P., Hirahara, S., Horányi, A., Muñoz-Sabater, J., Nicolas, J., Peubey, C.,
689   Radu, R., Schepers, D., Simmons, A., Soci, C., Abdalla, S., Abellan, X., Balsamo, G., Bechtold, P., Biavati,
690   G., Bidlot, J., Bonavita, M., De Chiara, G., Dahlgren, P., Dee, D., Diamantakis, M., Dragani, R., Flemming,
691   J., Forbes, R., Fuentes, M., Geer, A., Haimberger, L., Healy, S., Hogan, R. J., Hólm, E., Janisková, M.,
692   Keeley, S., Laloyaux, P., Lopez, P., Lupu, C., Radnoti, G., de Rosnay, P., Rozum, I., Vamborg, F., Villaume,
693   S., and Thépaut, J.-N.: The ERA5 global reanalysis, Q. J. Roy. Meteor. Soc., 146, 1999– 2049,
694   https://doi.org/10.1002/qj.3803, 2020 Ishizu, M., Miyazawa, Y., Tsunoda, T., and Guo, X.: Seasonal
695   variability in the inorganic ocean carbon cycle in the Northwest Pacific evaluated using a biogeochemical and
696   carbon model coupled with and operational ocean model, Clim. Change, 162, 877-902,
697   https://doi.org/10.1007/s10584-020-02779-2, 2020.

698 Ishizu, M., Miyazawa, Y., and Guo, X.: Long-term variations in ocean acidification indices in the northwest
699   Pacific from 1993 to 2018, Clim. Change, 168, https://doi.org/10.1007/ s10584-021-03239-1, 2021.

700 Jin, S., Wei, Z., Wang, D., and Xu, T.: Simulated and projected SST of Asian marginal seas based on CMIP6
701   models, Front. Mar. Sci., 10:1178974, https://doi.org/10.3389/fmars.2023.1178974, 2023.

702 Jochum, M., Yeager, S., Lindsay, K., Moore, K., and Murtugudde, R.: Quantification of the feedback between
703   phytoplankton and ENSO in the community climate system model, J. Clim., 23, 2916–2925,
704   https://doi.org/10.1175/2010JCLI3254.1, 2009.

705 Jung, H. K., Rahman, S. M., Kang, C.-K., Park, S.-Y., Lee, S. H., and Park, H. J.: The influence of climate
706   regime shifts on the marine environment and ecosystems in the East Asian Marginal Seas and their
707   mechanism, Deep-Sea Res. II, 143, 110-120, https://doi.org/10.1016/j.dsr2.2017.06.010, 2017.

708 Jung, H.-C, Moon, B.-K., Lee, H., Choi, J.-H., Kim, H.-K., Park, J.-Y., Byun, Y.-H., Lim, Y.-J., and Lee, J.:
709   Development and assessment of NEMO(v3.6) –TOPAZ(v2), a coupled global ocean biogeochemistry model,
710   Asia-Pac. J. Atmos. Sci., 56, 411-428, https://doi.org/10.1007/s13143-019-00147-4, 2020.

711 Kang, X., Zhang, R.H., Gao, C., and Zhu, J.: An improved ENSO simulation by representing chlorophyll-
712   induced climate feedback in the NCAR community earth system model, Sci. Rep., 7, 1-9,
713   https://doi.org/10.1038/s41598-017-17390-2, 2017.

714 Kawai., H.: Hydrography of Kuroshio extension, in: Kuroshio: Its Physical Aspects, edited by: Stommel, H. and
715   Yoshida, K., University of Tokyo Press, 235–352, 1972.

716 Kim, G.E., Gnanadesikan, A., and Pradal, M.A.: Increased surface ocean heating by colored detrital matter (CDM)
717   linked to greater Northern Hemisphere ice formation in the GFDL CM2MC ESM. J. Climate, **29**(24), 9063–
718   9076. https://doi.org/10.1175/ jcli-d-16-0053.1, 2016.

719 Kuroda, H., Toya, Y., Watanabe, T., Nishioka, J., Hasegawa, D., Taniuchi, Y., and Kuwata, A.: Influence of
720   Coastal Oyashio water on massive spring diatom blooms in the Oyashio area of the North Pacifc, Ocean. Prog
721   Oceanogr., 175, 328–344. https://doi.org/10.1016/j.pocean.2019.05.004, 2019.

722 Kwon, K.M.: A numerical experiment on the currents along the eastern boundary of the Yellow Sea in summer
723   2007. M.D Thesis, Kunsan National University, 89p.

724 Large, W. G., McWilliams, J. C., and Doney, S. C.: Ocean vertical mixing: a review and a model with a nonlocal
725   boundary layer parameterization, Rev. Geophys., 32, 363–403, https://doi.org/10.1029/94RG01872, 1994.

726 Lauvset, S. K., Key, R. M., Olsen, A., van Heuven, S., Velo, A., Lin, X., Schirnick, C., Kozyr, A., Tanhua, T.,
727   Hoppema, M., Jutterström, S., Steinfeldt, R., Jeansson, E., Ishii, M., Perez, F. F., Suzuki, T., and Watelet, S.: A
728   new global interior ocean mapped climatology: the 1° × 1° GLODAP version 2, Earth Syst. Sci. Data, 8, 325–
729   340, https://doi.org/10.5194/essd-8-325-2016, 2016.

730 Lee, D.-G., Oh, J.-H., Noh, K. M., Kwon, E. Y., Kim, Y. H., and Kug, J.-S.: What controls the future phytoplankton
731   change over the Yellow and East China Seas under global warming?, Front. Mar. Sci., 10:1010341,
732   https://doi.org/10.3389/fmars.2023.1010341, 2023.

733 Lee, H., Moon, B.-K., Jung, H.-C., Park, J.-Y., Shim, S., La, N., Kim, A.-H., Yum, S.S., Ha, J.-C., Byun, Y.-H.,
734   Sung, H.M., and Lee, J.: Development of the UKESM-TOPAZ Earth System Model (Version 1.0) and
735   preliminary evaluation of its biogeochemical simulations, Asia-Pac. J. Atmos. Sci., 58(3), 379-400,
736   https://doi.org/10.1007/s13143-021-00263-0, 2022.

737 Lembke-Jene, L, Tiedemann, R., Nürnberg, D., Kokfelt, U., Kozdon, R., Max, L., Röhl, U., and Gorbarenko, A.:
738   Deglacial variability in Okhotsk Sea Intermediate Water ventilation and biogeochemistry: Implications for
739   North Pacific nutrient supply and productivity, Quat. Sci. Rev., 160, 116-137,
740   https://doi.org/10.1016/j.quascirev.2017.01.016, 2017.

741 Ma, S., Tian, Y., Li, J., Yu, H., Cheng, J., Sun, P., Fu, C., Liu, Y., and Watanabe, Y.: Climate variability patterns
742   and their ecological effects on ecosystems in the Northwestern North Pacific, Front. Mar. Sci., 7, 546882,
743   https://doi.org/10.3389/fmars.2020.546882, 2020.

744 Mauri, E., Poulain, P., Juznic-Zonta, Z.: MODIS chlorophyll variability in the northern Adriatic Sea and
745   relationship with forcing parameters, J. Geophys. Res., 112, 1–14, https://doi.org/10.1029/2006JC003545,
746   2007

747 Manizza, M., Le Quéré, C., Watson, A.J., Buitenhuis, E.T.: Bio-optical feedbacks among phytoplankton, upper
748   ocean physics and sea-ice in a global model. Geophys. Res. Lett. 32, L05603,
749   https://doi.org/10.1029/2004GL020778, 2005.

750 McWilliams, J. C.: Targeted coastal circulation phenomena in diagnostic analyses and forecast, Dynam. Atmos.
751   Oceans, 49, 3–15, https://doi.org/10.1016/j.dynatmoce.2008.12.004, 2009.

752 Mellor, G. L. and Yamada, T.: Development of a turbulence closure model for geophysical fluid problems, Rev.
753   Geophys., 20, 851– 875, https://doi.org/10.1029/RG020i004p00851, 1982.

754 Moon, J.H., Hirose, N., and Yoon, J.-H.: Comparison of wind-tidal contributions to seasonal circulation of the
755   Yellow Sea, J. Geophys. Res., 114,   https://doi.org/10.1029/2009JC005314, 2009.

756 Na, R., Rong, Z., Wang, Z.A., Liang, S., Liu, C., Ringham, M., and Liang, H.: Air-sea CO_2 fluxes and cross-
757   shelf exchange of inorganic carbon in the East China Sea from a coupled physical-biogeochemical model,
758   Sci. Total Environ., 906, 167572, https://doi.org/10.1016/j.scitotenv.2023.167572, 2024.

759 Najjar, R. and Orr, J. C.: Design of OCMIP-2 simulations of chlorofluorocarbons, the solubility pump and
760   common biogeochemistry, Internal OCMIP Report, LSCE/CEA Saclay, Gif-surYvette, France 1998.

761 Nishioka, J., Obata, H., Ogawa, H., Ono, K., Yamashita, Y., Lee, K., Takeda, S., and Yasuda, I.: Subpolar
762   marginal seas fuel the Norh Pacific through the intermediate water at the termination of the global ocean
763   circulation, P. Natl. Acad. Sci. USA, 117, 12665–12673, https://doi.org/10.1073/pnas.2000658117, 2020.

764 Nishioka, J., Obata, H., Hirawake, T., Kondo, Y., Yamashita, Y., Misumi, K., and Yasuda, I.: A review: iron and
765   nutrient supply in the subarctic Pacific and its impact on phytoplankton production, J. Oceanogr., 77, 561-
766   587, https://doi.org/10.1007/s10872-021-00606-5, 2021.

767 Nitani, H.: Beginning of the Kuroshio, in: Kuroshio: Its Physical Aspects, edited by: Stommel, H. and Yoshida,
768   K., University of Tokyo Press, 129–163, 1972.

769 Overland, J., Rodionov, S., Minobe, S., and Bond, N.: North Pacific regime shifts: definitions, issues and recent
770   transitions, prog, oceanogr., 77, 92-102, https://doi.org/10.1016/j.pocean.2008.03.016, 2008.

771 Qui, B.: Kuroshio and Oyashio currents, in: edited by Steele, J. H., Thorpe, S. A., Turekian, K. K., Encyclopedia
772   of Ocean Sciences. Academic, London, 1413-1425, https://doi.org/10.1006/rwos.2001.0350, 2001

773 Park, J.-Y., Kug, J.-S., Seo, H., and Bader, J.: Impact of bio-physical feedbacks on the tropical climate in
774   coupled and uncoupled GCMs, Clim. Dyn., 43, 1811-1827, https://doi.org/10.1007/s00382-013-2009-0, 2014.

775 Park, J.-Y., Dunne, J.P., and Stock, C.A.: Ocean chlorophyll as a precursor of ENSO: An Earth system modeling
776   study, Geophys. Res. Lett., 45, 1939-1947, https://doi.org/10.1002/2017GL076077, 2018.

777 Park, J.-Y., Stock, C.A., Dunne, J.P., Yang, X., and Rosati, A.: Seasonal to multiannual marine ecosystem
778   prediction with a global earth system model. Science, 365, 284-288, DOI: 10.1126/science.aav6634, 2019.

779 Okamoto, S., Hirawake, T., and Saito, S.: Internal variability in the magnitude and timing of the spring bloom in
780   the Oyashio region, Deep Sea Res. II, 57, 1608-1617, https://doi.org/10.1016/j.dsr2.2010.03.005, 2010.

781 Reid, P.C., Fischer, A.C., Lewis-Brown, E., Meredith, M.P., Sparrow, M., Andersson, A.J., Antia, A., Bates,
782   N.R., Bathmann, U., Beaugrand, G., Brix, H., Dye, S., Edwards, M., Furevik, T., GangstØ, R., Hátún, H.,
783   Hopcroft, R.R., Kendall, M., Kasten, S., Keeling, R., Le Qur, C., Mackenzie, F.T., Malin, G., Mauritzen, C.,
784   Olafsson, J., Paull, C., Rignot, E., Shimada, K., Vogt, M., Wallace, C., Wang, Z., and Washington, R.: Chapter
785   1 Impacts of the Oceans on Climate Change. Academic Press, 56, 1-150, https://doi.org/10.1016/S0065-
786   2881(09)56001-4, 2009.

787 Séférian, R., Gehlen, M., Bopp, L., Resplandy, L., Orr, J.C., Marti, O., Dunne, J.P., Christian, J.R., Doney, S.C.,
788   Ilyina, T., Lindsay, K., Halloran, P.R., Heinze, C., Segschneider, J., Tjiputra, J., Aumont, O., and Romanou,
789   A.: Inconsistent strategies to spin up models in CMIP5: implications for ocean biogeochemical model
790   performance assessment. Geosci. Model Dev. 9, 1827–1851, https://doi.org/10.5194/gmd-9-1827-2016, 2016.

791 Shchepetkin, A. F. and McWilliams, J. C.: A method for computing horizontal pressure-gradient force in an
792   oceanic model with a nonaligned vertical coordinate, J. Geophys. Res., 108, 3090,
793   https://doi.org/10.1029/2001JC001047, 2003.

794 Shchepetkin, A. F. and McWilliams, J. C.: The regional oceanic modeling system (ROMS): a split-explicit, free-
795   surface, topography-following-coordinate oceanic model, Ocean Model., 9, 347–404,
796   https://doi.org/10.1016/j.ocemod.2004.08.002, 2005.

797 Shiozaki, T., Ito, S.-I., Takahashi, K., Saito, H., Nagata, T., and Furuya, K.: Regional variability of factors
798   controlling the onset timing and magnitude of spring algal blooms in the northwestern North Pacific, J.
799   Geophys. Res., 119, 253-265, https://doi. org/10.1002/2013JC009187, 2014.

800 Siswanto, E., Matsumoto, K., Honda, M. C., Fujiki, T., Sasaoka, K. and Saino, T.: Reappraisal of meridional
801   differences of factors controlling phytoplankton biomass and initial increase preceding seasonal bloom in the
802   northwestern Pacific Ocean. Remote Sensing of Envir., 159, 44-56, https://doi.org/10.1016/j.rse.2014.11.028,
803   2015.

804 Song, Y., and Haidvogel, D.: A semi-implicit ocean circulation model using a generalized topography following
805   coordinate system, J. Comput. Phys., 115, 228-244, https://doi.org/10.1006/jcph.1994.1189, 1994.

806 Song, Y. T. and Wright, D. G.: A general pressure gradient formulation for ocean models, Part II: Energy,
807   momentum, and bottom torque consistency, Mon. Weather Rev., 126, 3231–3247,
808   https://doi.org/10.1175/1520-0493(1998)126<3231:AGPGFF>2.0.CO;2, 1998.

809 Sugimoto, S., and Hanawa, K.: Roles of SST anomalies on the wintertime turbulent heat fluxes in the Kuroshio–
810   Oyashio confluence region: influences of warm eddies detached from the Kuroshio extension. J Clim.
811   https://doi.org/10.1175/2011jcli4023.1, 2011.

812 Taguchi, B., Xie, S.-P., Schneider, N., Nonaka, M., Sasaki, H., and Sasai, Y.: Decadal variability of the Kuroshio
813   Extension: Observations and an eddy-resolving model hindcast, J. Climate, 20, 2357–2377,
814   https://doi.org/10.1175/JCLI4142.1, 2007.

815 Takahashi, T., Sutherland, S. C., Wanninkhof, R., Sweeney, C., Feely, R. A., Chipman, D. W., Hales, B.,
816   Friederich, F., Chavez, F., Sabine, C., Watson, A., Bakker, D. C.E., Schuster, U., Metzl, N., Yoshikawa-Inoue,
817   H., Ishii, M., Midorikawa, T., Nojiri, Y., KÖrtzinger, A., Steinhoff, T., Hoppema, M., Olafsson, J., Arnarson,
818   T. S., Tilbrook, B., Johannessen, T., Olsen, A., Bellerby, R., Wong, C.S., Delille, B., Bates, N.R., and de Baar,
819   H. J.W.: Climatological mean and decadal change in surface ocean pCO2, and net sea-air CO2 flux over the
820   global oceans, Deep-Sea Res. II, 56, 554-577, 2009.

821 Taniguchi, A.: Differences in the structure of the lower trophic levels of pelagic ecosystems in the eastern and
822   western subarctic Pacific, Prog. in Oceanogra., 43, 289-315, https://doi.org/10.1016/S0079-6611(99)00011-7,
823   1999.

824 Taylor, K.E.: Summarizing multiple aspects of model performance in a single diagram, J. Geophys. Res.-Atmos.
825   106, 7183–7192, https://doi.org/10.1029/2000JD900719, 2001.

826 Taylor, K., Juckes, M., Balaji, V., Cinquini, L., Denvil, S., Durack, P., Elkington, M., Guilyardi, E., Kharin, S.,
827   Lautenschlager, M., Lawrence, B., Nadeau, D., and Stockhause, M.: CMIP6 Global Attributes, DRS,
828   Filenames, Directory Structure, and CV's, https://github.com/WCRP-CMIP/WGCM_Infrastructure_Panel/
829   blob/main/Papers/CMIP6_global_attributes_filenames_CVs_ v6.2.7.pdf (last access: 15 January 2021), 2018.

830 Umlauf, L., Burchard, H., and Hutter, K.: Extending the κ-ω turbulence model towards oceanic applications,
831   Ocean Model., 5, 195–218, 5. https://doi.org/10.1357/00222 4003322005087, 2003.

832 Wang, X., Luo, C., Ge, T., Xu, C., and Xum Y.: Controls on the sources and cycling of dissolved inorganic
833   carbon in the Chanjiang and Huanghe River estuaries, China: ^{14}C and ^{13}C studies, Limnol. And Oceanogra.,
834   61, 1358-1374, https://doi.org/10.1002/lno.10301, 2016.

835 Wang, Y., Kang, J., Sun, X., Huang, J., Lin, Y., and Xiang, P.: Spatial patterns of phytoplankton community and
836   biomass along the Kuroshio extension and adjacent water in late spring, Mar. Biol.,
837   https://doi.org/10.1007/s00227-021-03846-7, 2021.

838 Wang, Y., Bi, R., Zhang, J., Gao, J., Takeda, S., Kondo, Y., Chen, F., Jin, G., Sachs, J. P., and Zhao, M.:
839   Phytoplankton distributions in the Kuroshio-Oyashio Region of the Northwest Pacific Ocean: Implications for
840   marine ecology and carbon cycle, Front. Mar. Sci., 9, 865142, https://doi.org/10.3389/fmars.2022.865142,
841   2022.

842 Wanninkhof, R.: Relationship between wind speed and gas exchange over the ocean. J. Geophys. Res. 97, 7373–
843   7382m https://doi.org/10.1029/92JC00188, 1992.

844 Watson A. J.: Iron limitation in the oceans. In The Biogeochemistry of Iron in Seawater, Turner DR, Hunter KA
845   (eds). Wiley: Chichester; 9–39, 2001.

846 Weatherall, P., Marks, K. M., Jakobsson, M., Schmitt, T., Tani, S., Arndt, J. E., Rovere, M., Chayes, D., Ferrini,
847   V., and Wigley, R.: A new digital bathymetric model of the world's oceans, Earth Space Sci., 2, 331–345,
848   https://doi.org/10.1002/2015EA000107, 2015.

849 Wu, Q., Wang, X., He, Y., and Zheng, J.: The relationship between chlorophyll concentration and ENSO events
850   and possible mechanisms off the Changjiang River estuary, Remote Sens., 15, 2384,
851   https://doi.org/10.3390/rs15092384, 2023.

852 Yasuda, I.: Hydrographic structure and variability in the Kuroshio–Oyashio transition area, J. Oceanogr., 59,
853   389–402, https://doi.org/10.1023/A: 1025580313836, 2003.

854 Yatsu, A., Chiba, S., Yamanaka, Y., Ito, S., Shimizu, Y., and Kaeriyama, M.: Climate forcing and the
855   Kuroshio/Oyashio ecosystem, ICES J. Mar. Sci., 70, 922-933, https://doi.org/10.1093/icesjms/fst084, 2013.

856 Zhai, W.-D., Dai, M.-H., and Guo, X.-H.: Carbonate system and CO_2 degassing fluxes in the inner estuary of
857   Changjiang (Yangtze) River, China. Mar. Chem., 107, 342-356,
858   https://doi.org/10.1016/j.marchem.2007.02.011, 2007.

859 Zhang, H.-R., Wang, Y., Xiu, P., Qi, Y., and Chai, F. (2021b). Roles of iron limitation in phytoplankton dynamics
860   in the Western and Eastern subarctic pacific, Front. Mar. Sci., 8. https://doi.org/10.3389/fmars.2021.735826,
861   2021.

862 Zhao, H., Dai, M., Gan, J., Zhao, X., Lu, Z., Liang, L., Liu, Z., Su, J., and Cao, Z.: River-dominated pCO_2
863   dynamics in the northern South China Sea during summer: A modeling study, Prog. Oceanogr., 190, 102457,
864   https://doi.org/10.1016/j.pocean.2020.102457, 2021.

865 Zhu, K., Chen, X., Mao, K., Hu, D., Hong, S., and Li, Y.: Mixing characteristics of the subarctic front in the
866   Kuroshio-Oyashio confluence region. Oceanologia., 61, 103–113,
867   https://doi.org/10.1016/j.oceano.2018.07.004, 2019.

868 Zhou, M.J., Shen, Z.L., and Yu, R.C.: Responses of a coastal phytoplankton community to increased nutrients
869   input from the Changjiang (Yangtze) River, Cont. Shelf Res., 28, 1483-1489,
870   https://doi.org/10.1016/j.csr.2007.02.009, 2008.

871

872

873
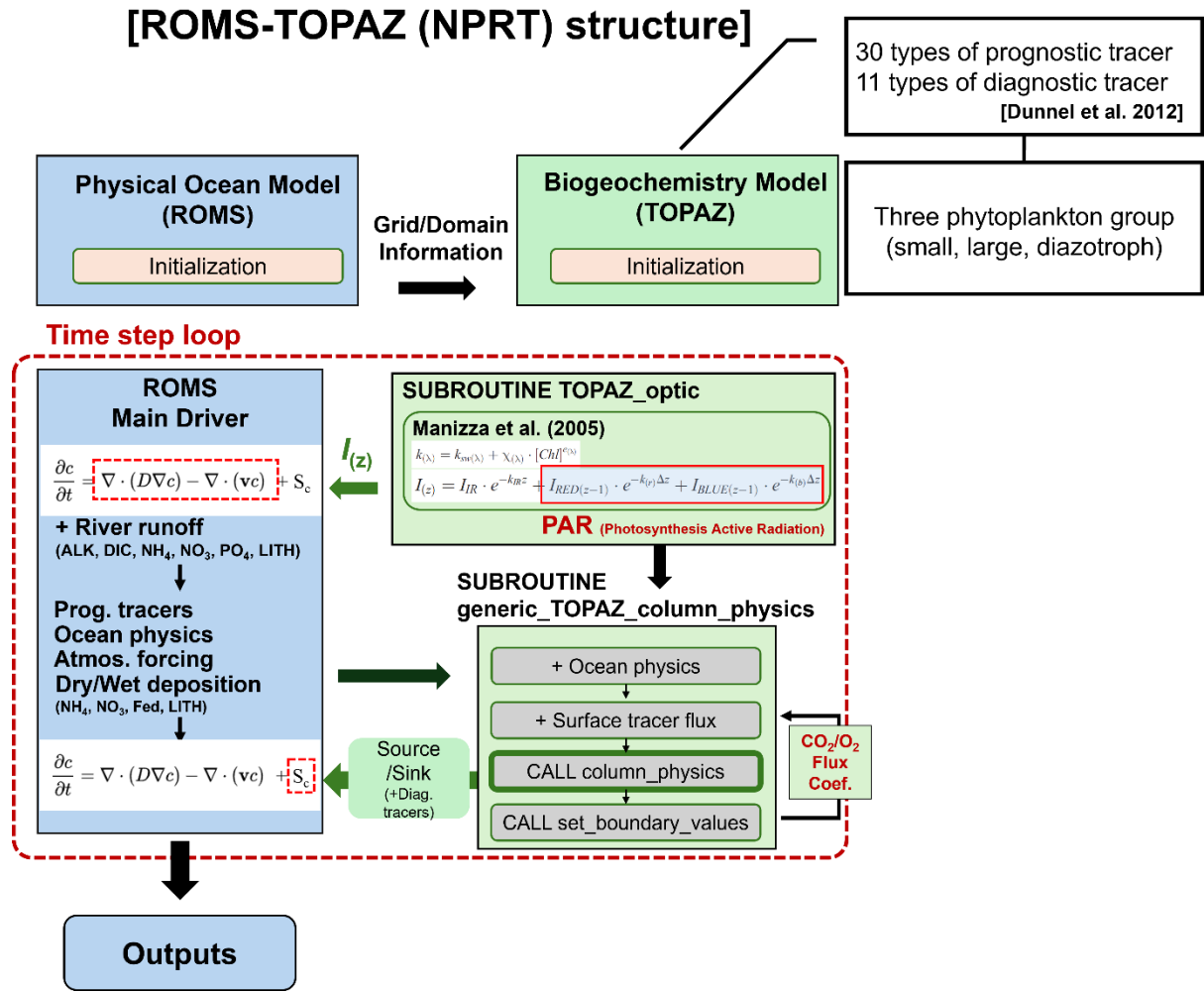
Fig. 1. Flow diagram of the ROMS–TOPAZ model (NPRT). Blue (green) boxes represent the ocean physical (biogeochemical) module. The black arrows indicate the process of transferring oceanic physical information to biogeochemical modules, and the green arrows represent vice versa process.

878

879
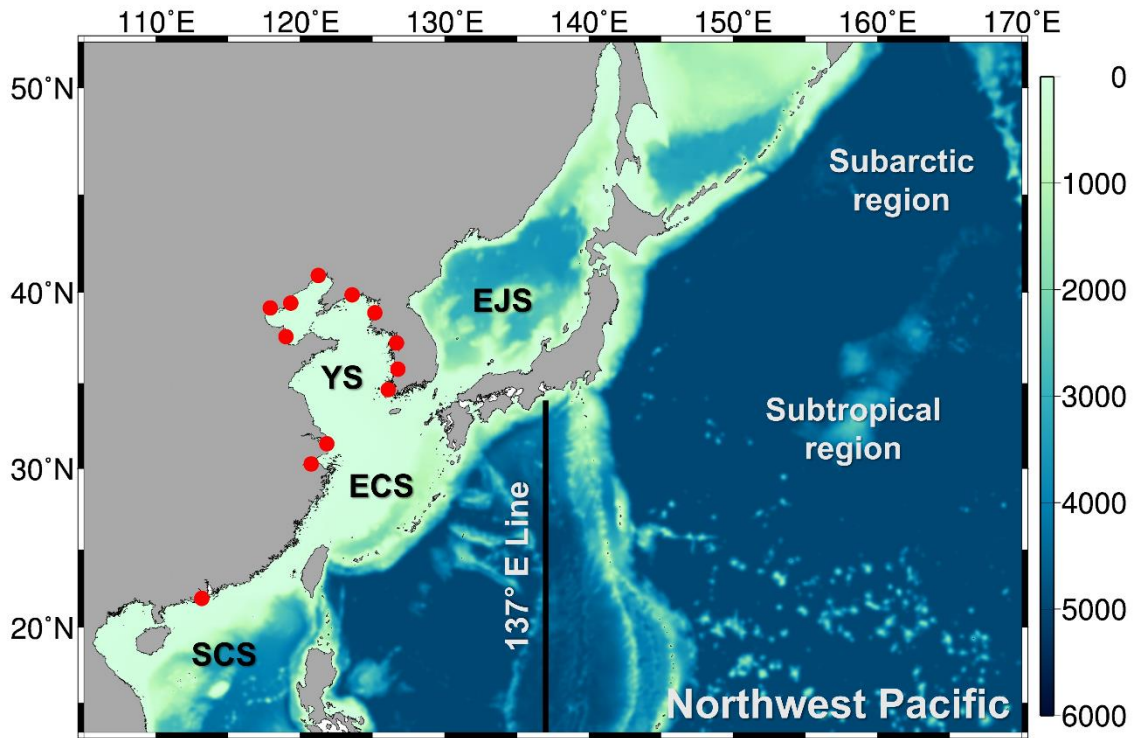
880 **Fig. 2.** Model domain and bottom topography for NPRT coupled modeling system. EJS:

881 East/Japan Sea, YS: Yellow Sea, ECS: East China Sea, SCS: South China Sea.   The red

882 circles indicate river runoff points, and the black line (137° E line) is the observation line of

883 the Japanese Meteorological Agency (JMA).

884

885

886

887

888

889

890
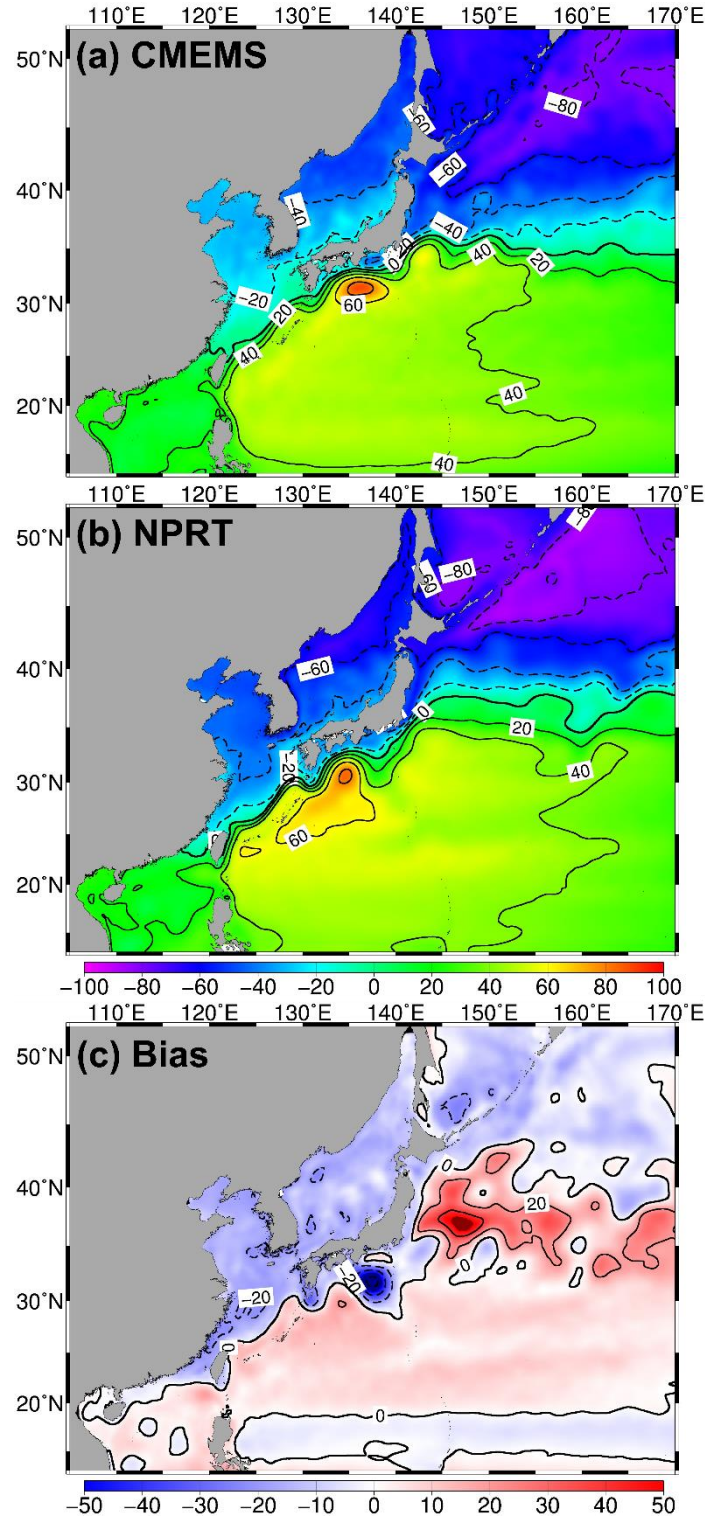
Fig. 3. Distributions of the annual mean sea surface height (SSH; cm) in (a) satellite altimeters

(CMEMS), (b) NPRT, and (c) biases between NPRT and observations (WOA18) from 2005

to 2014. To compare the two datasets, the spatial mean was subtracted from each one.

894
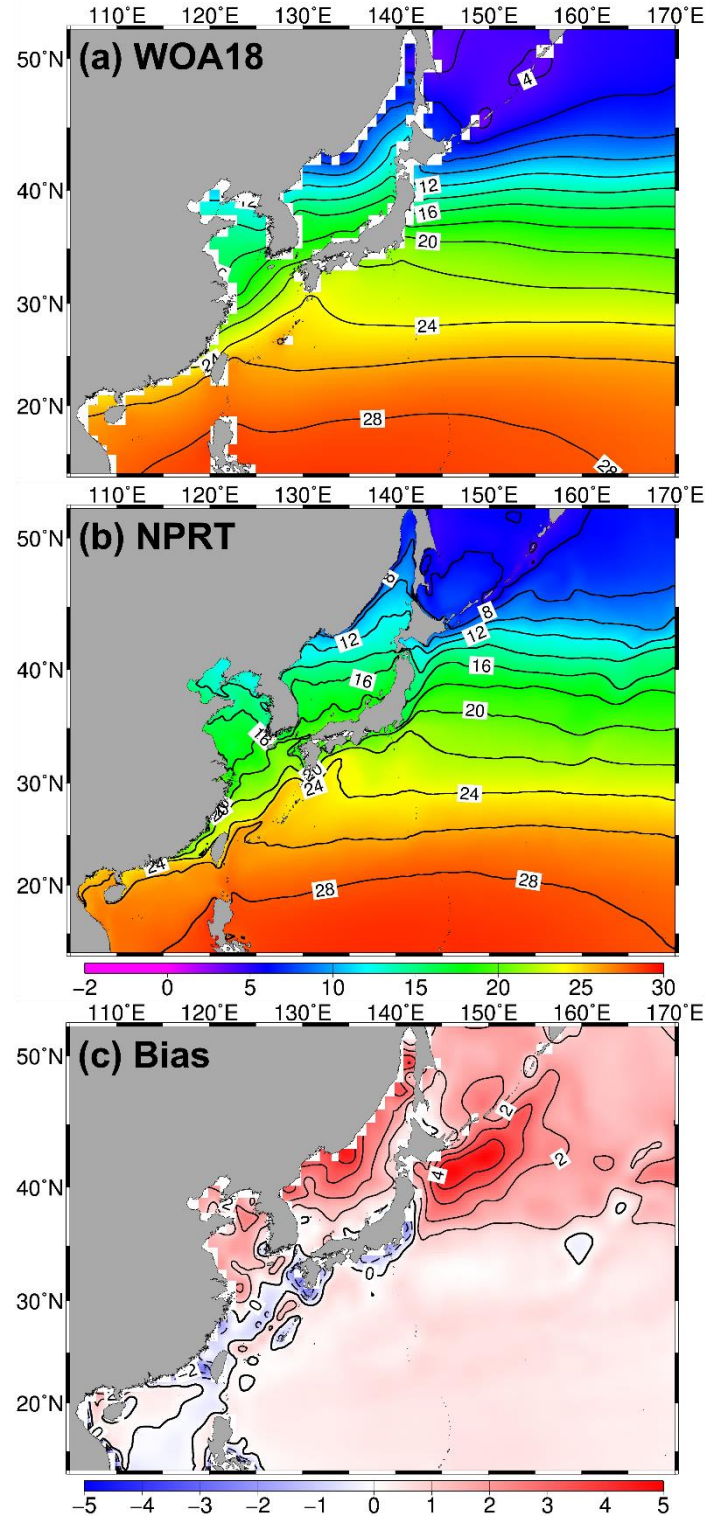
895   **Fig. 4.** Same as Fig. 3, except to in the annual mean sea surface temperature (SST) from (a)

896   World Ocean Atlas 2018 (WOA18), (b) NPRT, and (c) bias (NPRT – WOA18).

897

898
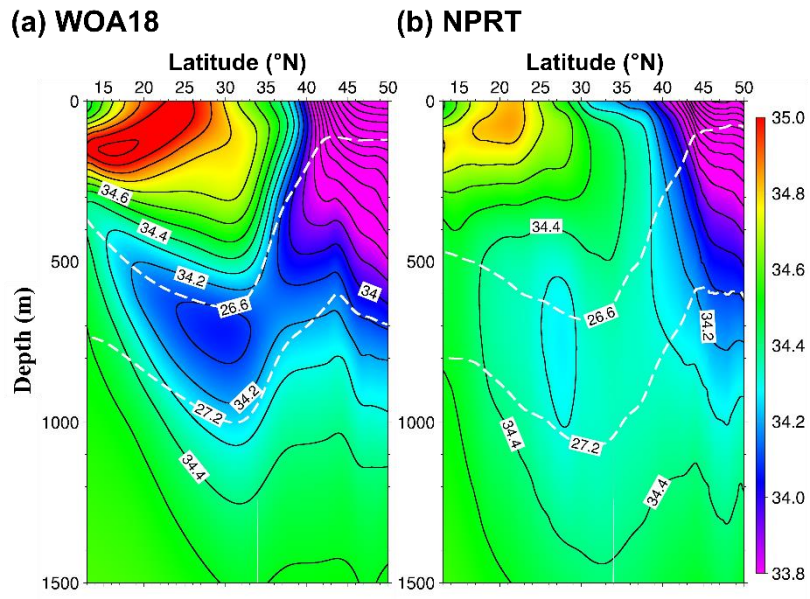
899 **Fig. 5.** Vertical structures of the climatological zonally averaged annual mean salinity between

900 145° E and 160° E in (a) the WOA18 data and (b) NPRT. The white dashed lines represent

901 potential 26.6 σ_θ and 27.2 σ_θ isopycnals, corresponding to the NPIW density range.

902

903
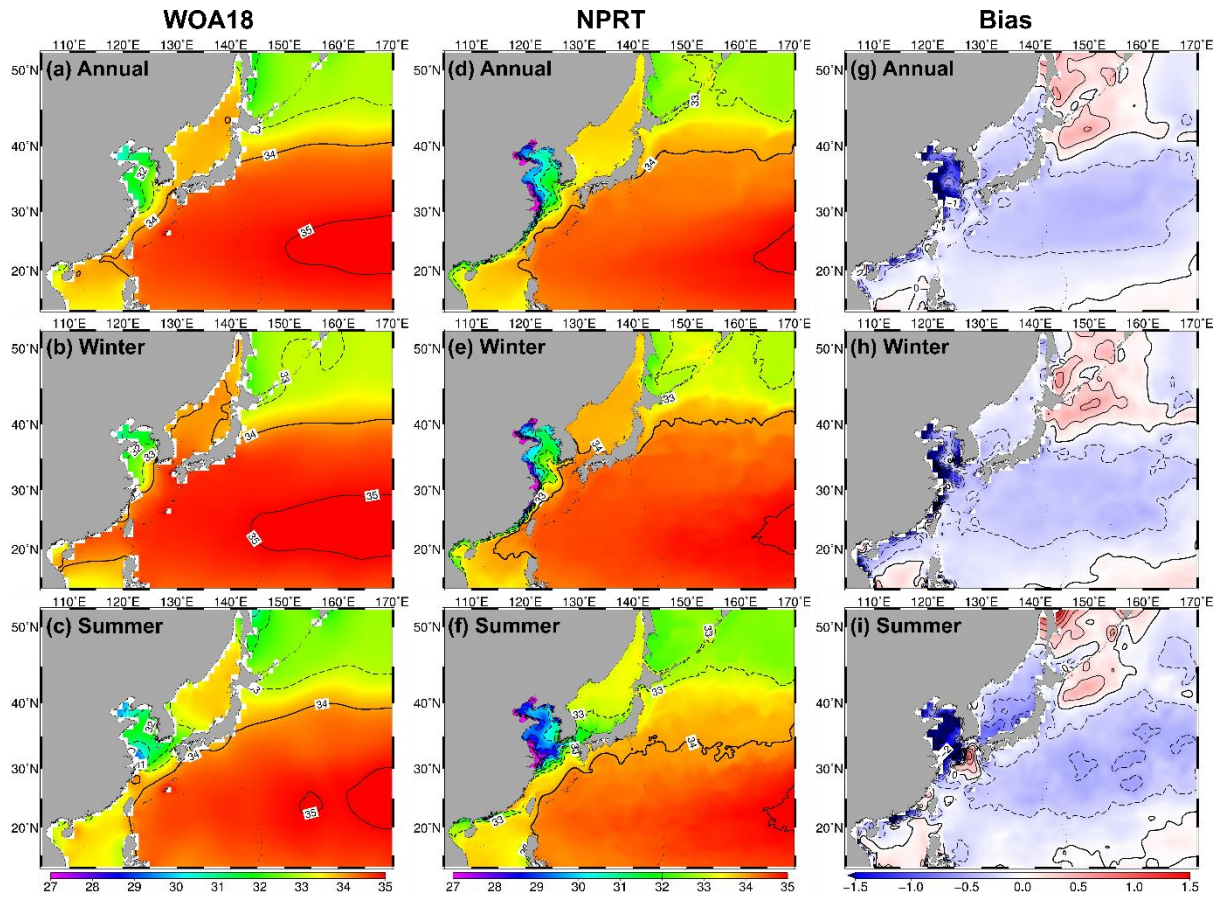
Fig. 6. Distributions of the surface salinity in (a, b, c) the WOA18 data, (d, e, f) NPRT, and (g,

905   h, i) biases for (a, d, g) the climatological mean, (b, e, h) winter and (c, f, i) summer.

906

907
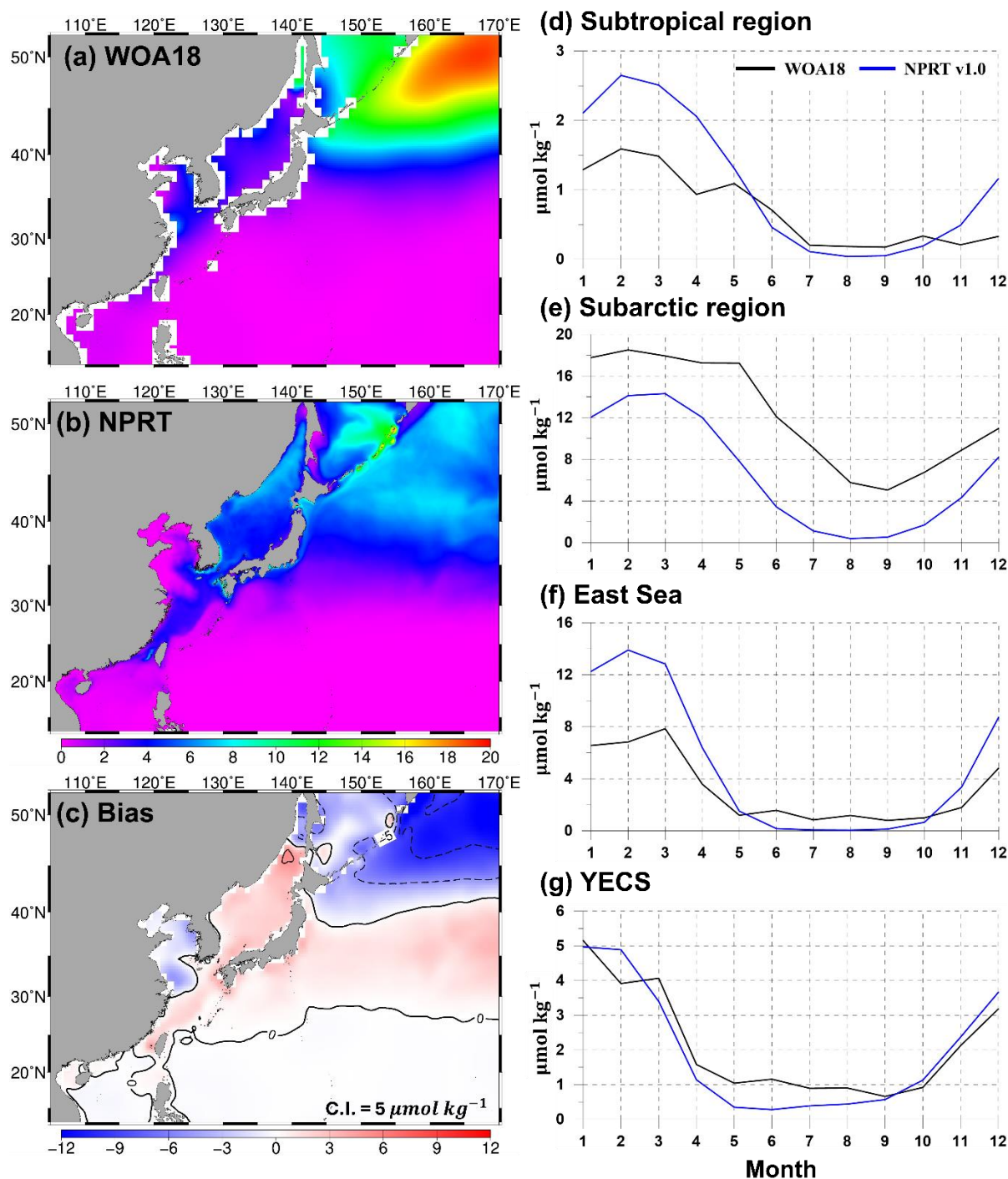
Fig. 7. Horizontal distributions of the annual mean surface nitrate concentrations (μmol kg⁻¹)
in (a) WOA18, (b) NPRT, and (c) biases between NPRT and observations (WOA18), and
seasonal variations in (d) the subtropical region (south of 40° N in the Northwest Pacific),
(e) the subarctic region (north of 40° N in the Northwest Pacific), (f) the East Sea, and (g)
the Yellow and East China Seas (YECS).

913
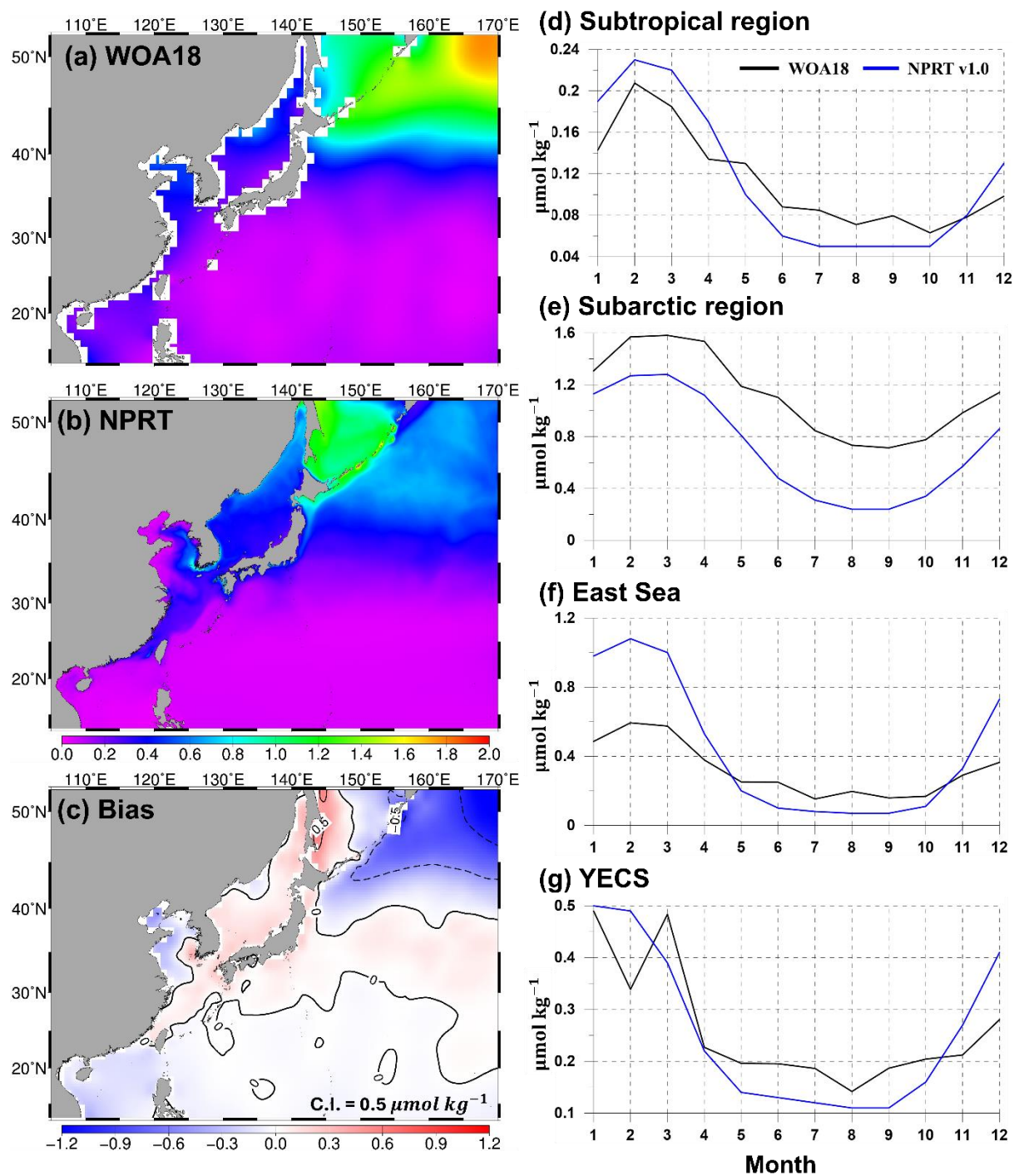
914 **Fig. 8.** Same as Fig. 7 except to the annual mean surface phosphate concentration (μmol kg⁻¹).

915

916

917

918
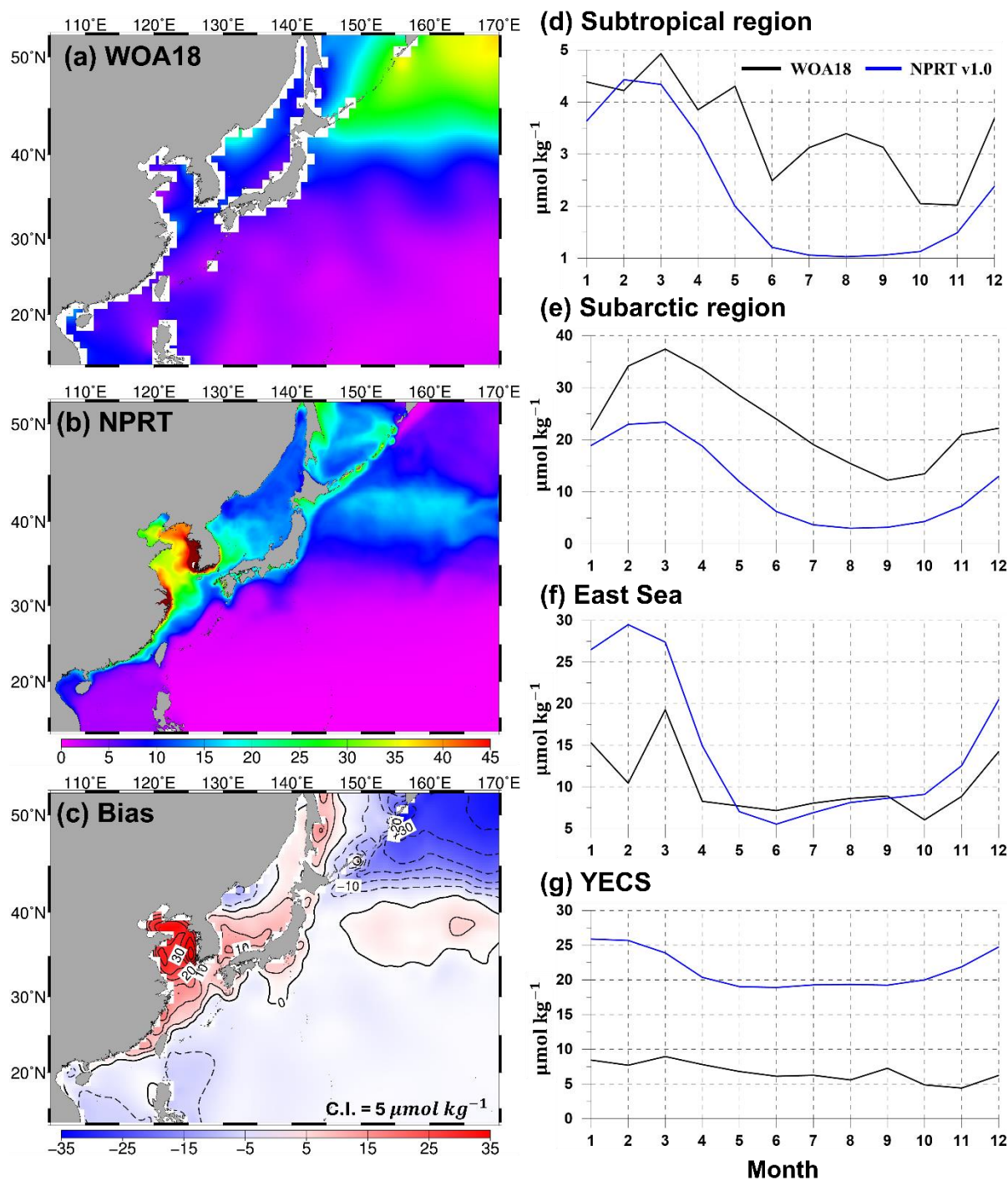
Fig. 9. Same as Fig. 7 except to the annual mean surface silicate concentration (μmol kg⁻¹).

920

921

922
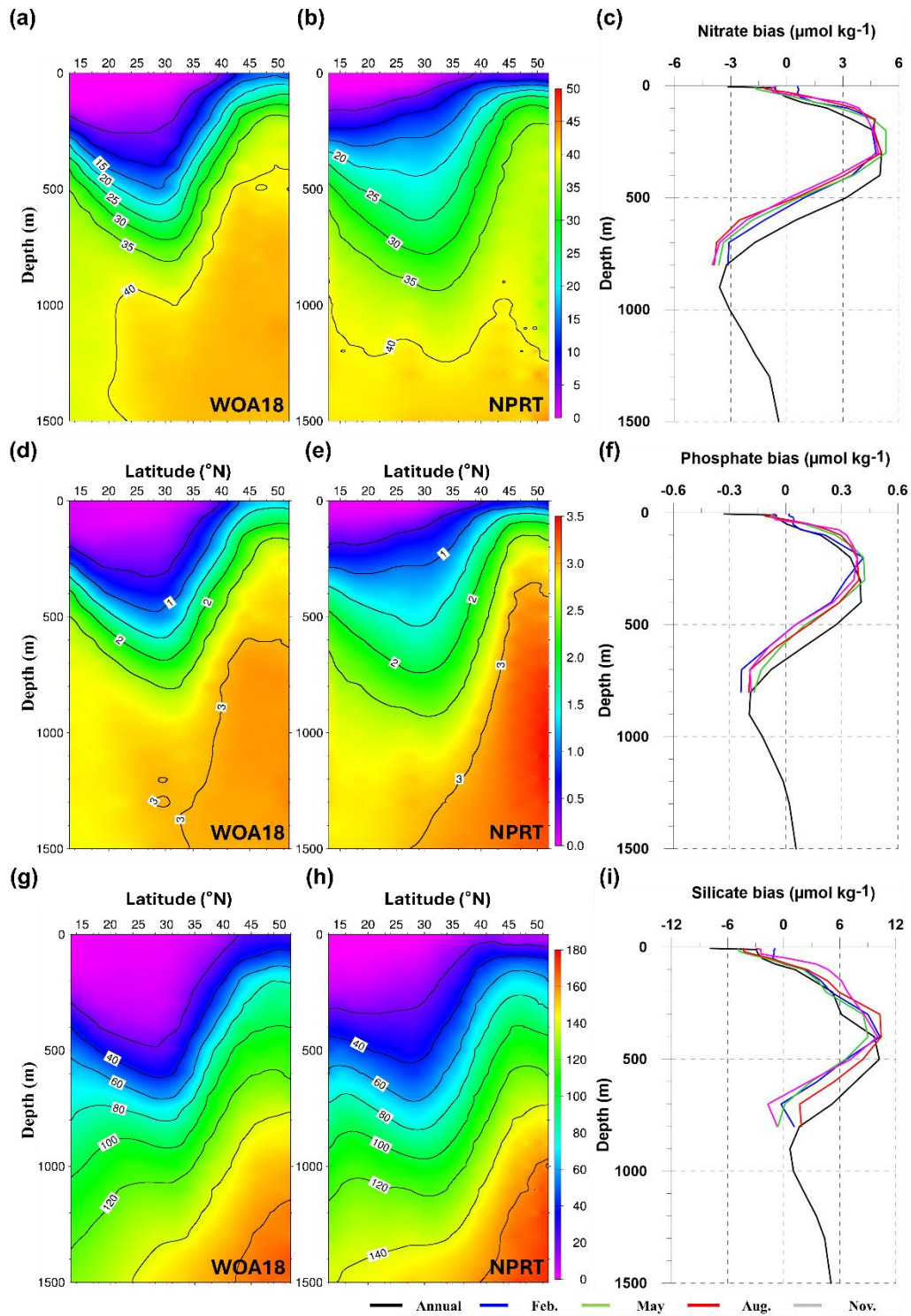
Fig. 10. Vertical structures of the zonal averaged annual mean (a, b) nitrate, (d, e) phosphate, and (g, h) silicate concentrations (μmol kg⁻¹) in the Northwest Pacific. The vertical profile of annual and monthly biases between observation and NPRT results for (c) nitrate, (f) phosphate, and (i) silicate.

927
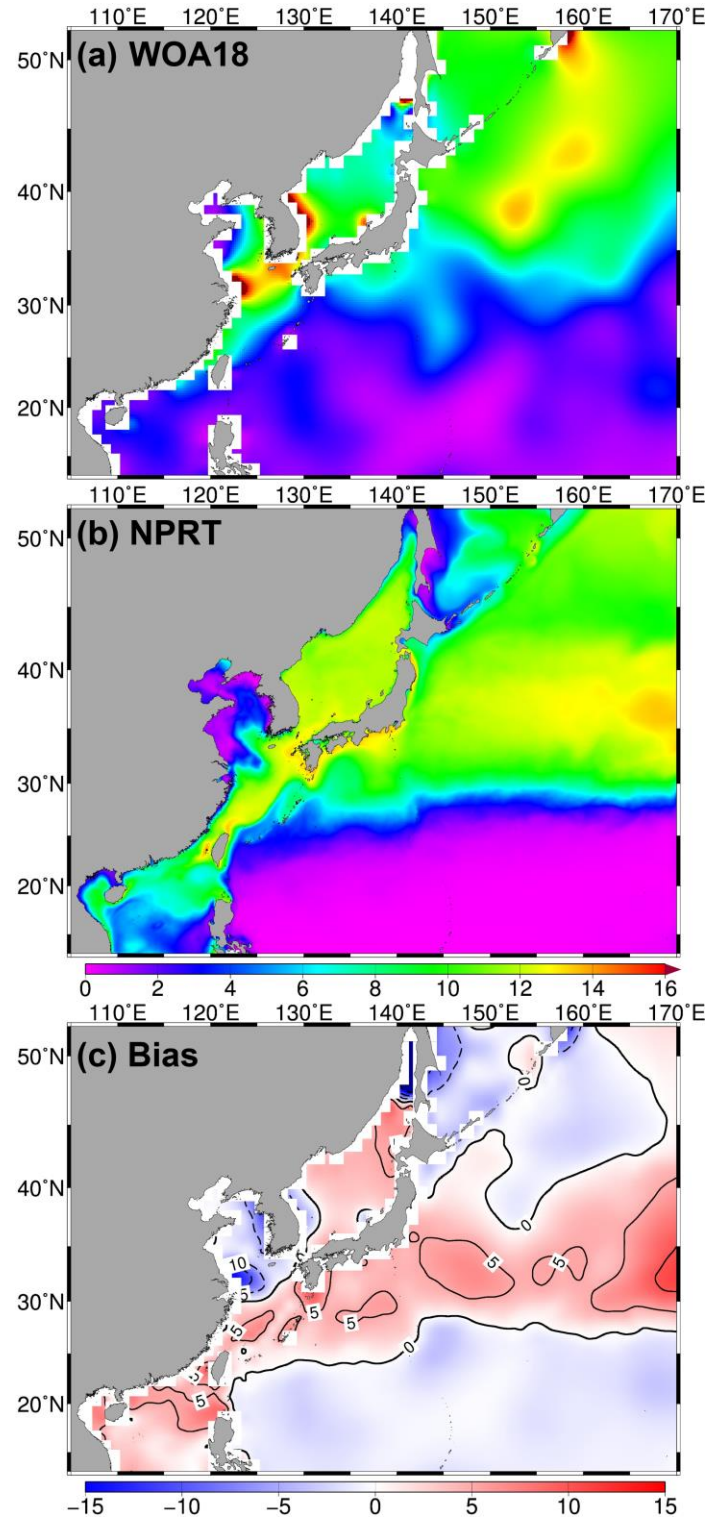
Fig. 11. Same as Fig. 3, except to in the annual mean surface N:P molar ratio.

929

930

931

932
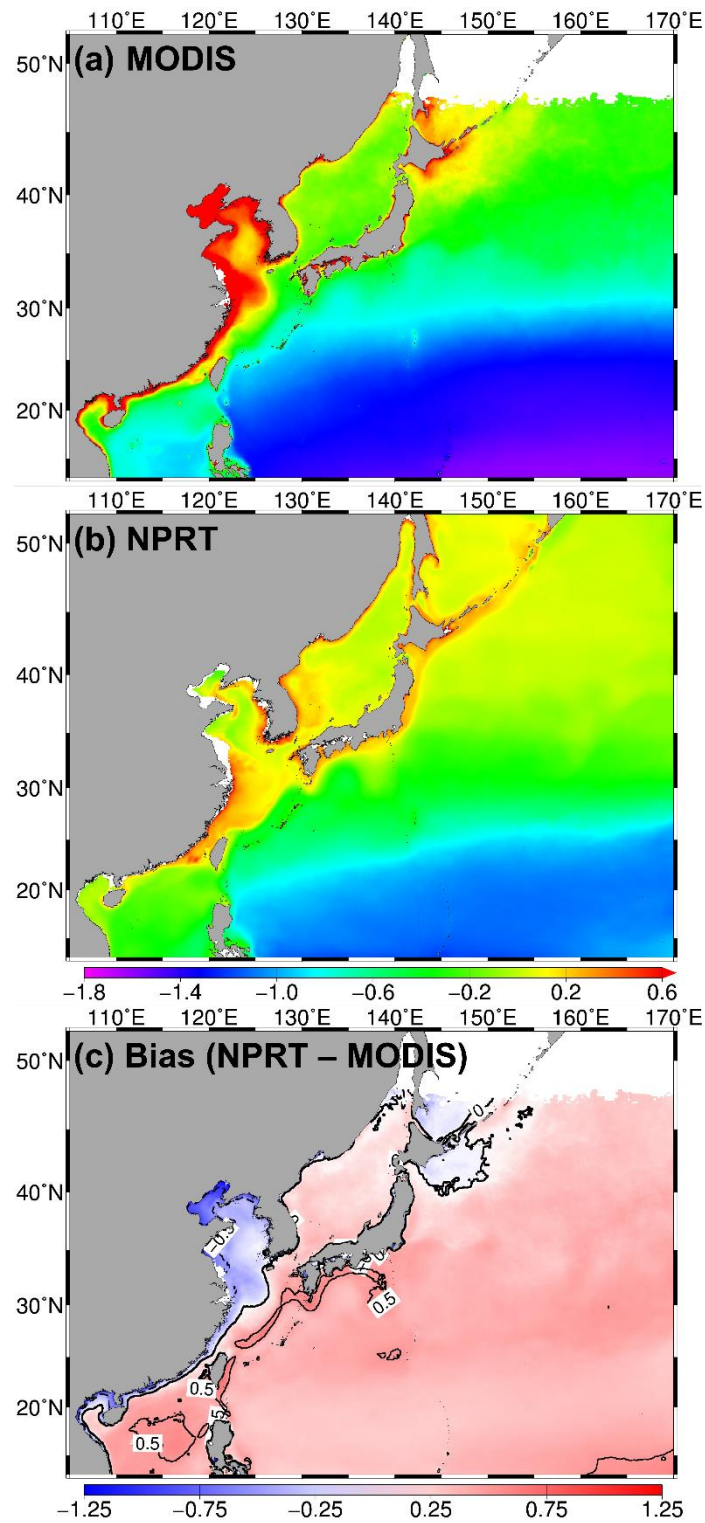
Fig. 12. Logarithm of the climatological annual-mean surface chlorophyll concentrations (μmol kg⁻¹) from (a) MODIS, (b) NPRT, (c) bias of between NPRT and observation (MODIS).

935
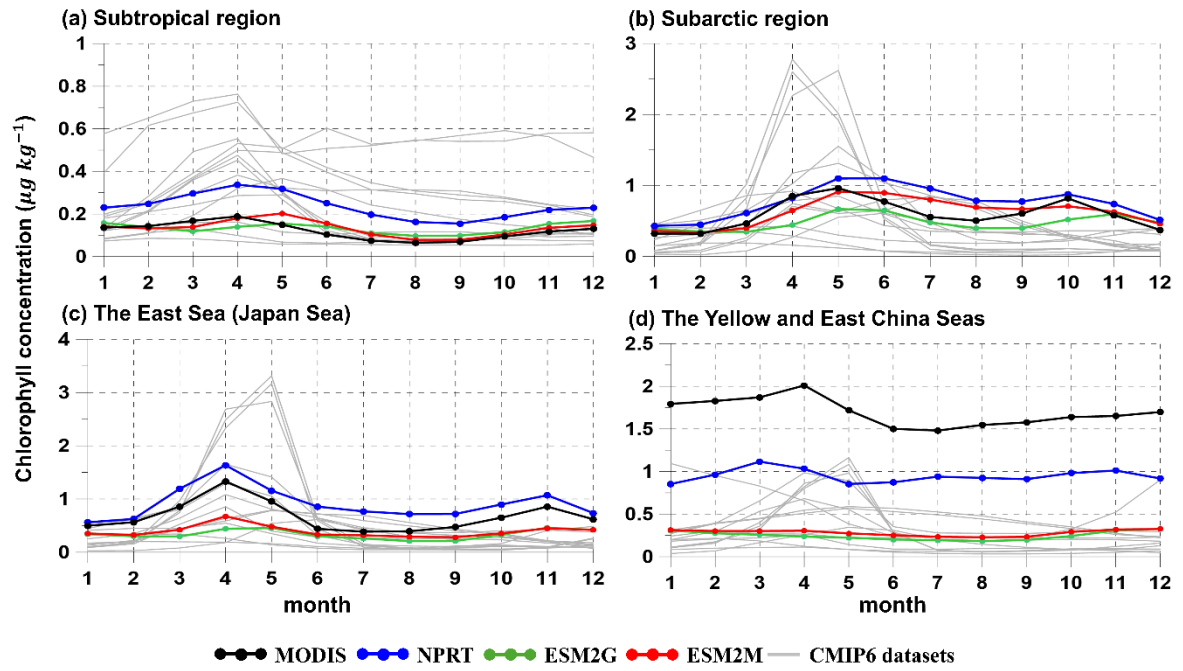
Fig. 13. Seasonal variations of the spatial averaged chlorophyll concentrations (μmol kg⁻¹) in

(a) the subtropical and (b) subarctic regions, (c) the East Sea, and (d) the YECS. Black,

blue, green, red and light grey lines indicate MODIS, NPRT, GFDL–ESM2G, GFDL–

ESM2M, and each ensemble model in CMIP6, respectively.
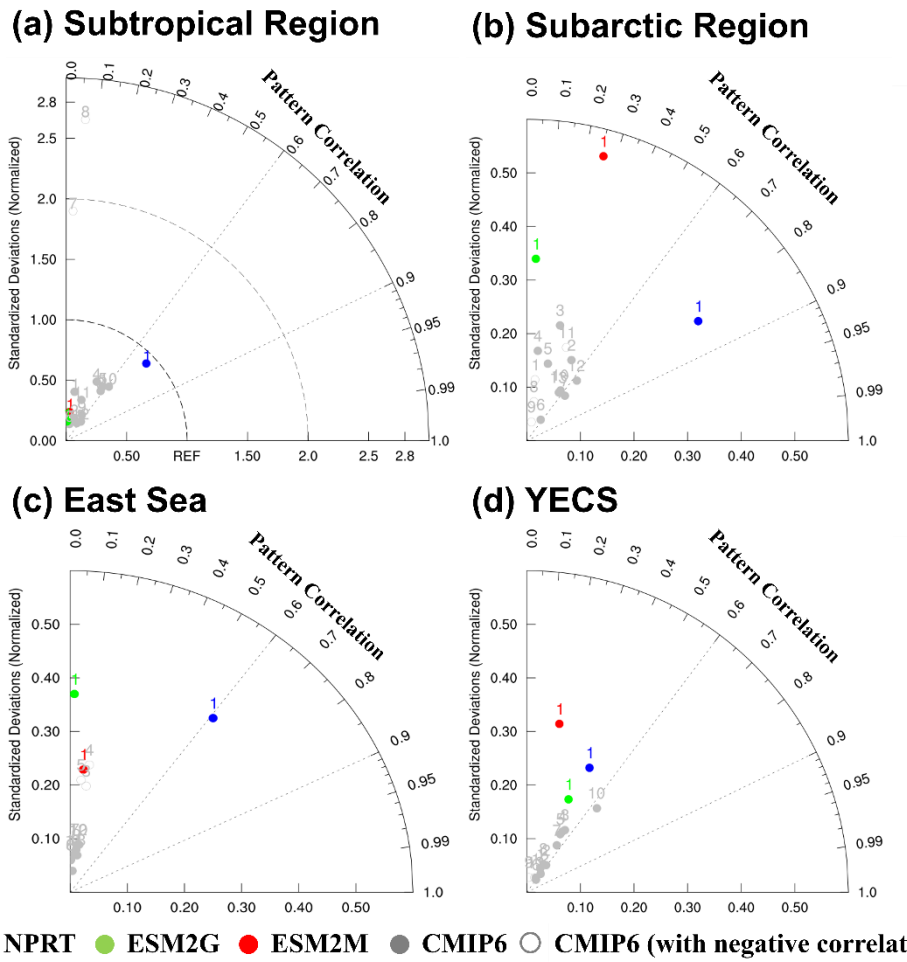
Fig. 14. Taylor diagrams (Taylor, 2001) of spatial four models (NPRT (blue dots), GFDL–ESM2G (green dots), GFDL–ESM2M (red dots) and each ensemble model in CMIP6 (grey dots)) for surface chlorophyll concentrations compared to observation (MODIS) at each region. The grey open dots (○) in CMIP6 indicate a negative pattern correlation. Taylor diagrams for time were calculated by comparing observational data with annual mean simulated fields of four models (NPRT, GFDL–ESM2G, GFDL–ESM2M and each ensemble in CMIP6) in the (a) subtropical and (b) subarctic regions, (c) East Sea, and (d) YECS, and the numbers represent each ensemble model in Table 1.
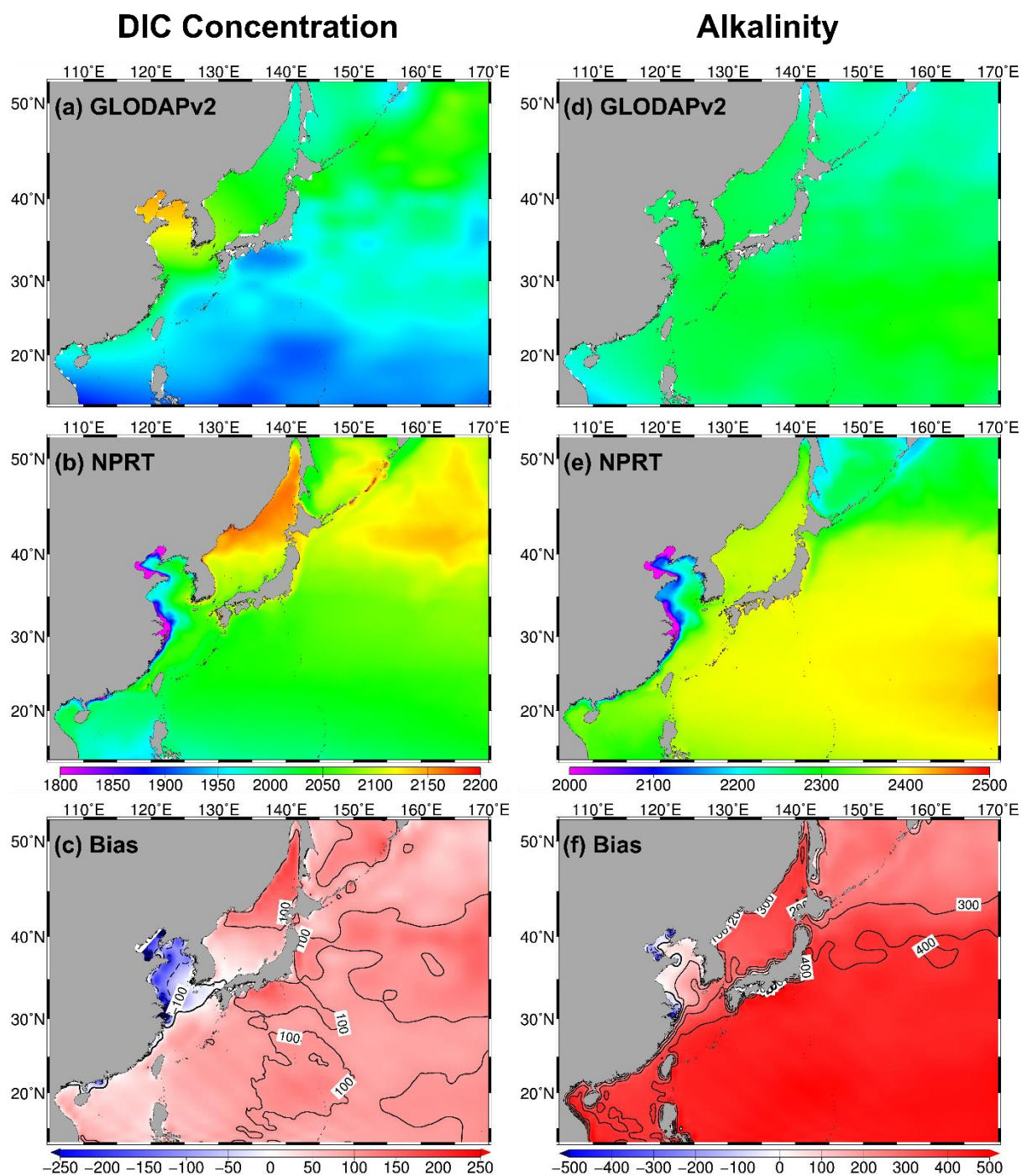
Fig. 15. Horizontal distributions of annual mean surface dissolved inorganic carbon (DIC; left panels) concentrations ($\mu mol\ kg^{-1}$) and alkalinity ($\mu mol\ kg^{-1}$; right panels) in the (a, d) GLODAPv2 and (b, e) NPRT in the Northwest Pacific. Biases (c, f) represent NPRT minus observation (GLODAPv2).

957

958
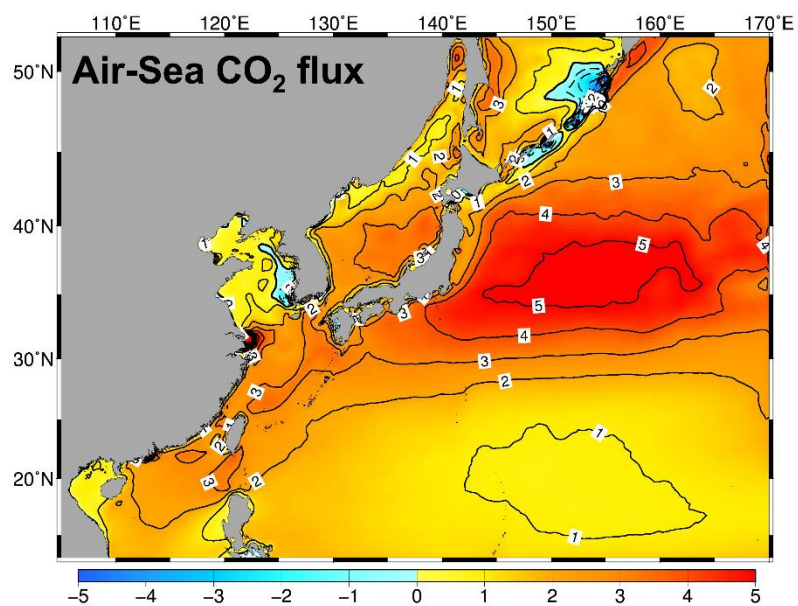
Fig. 16. Distribution of the annual mean air–sea CO_2 flux (mol m^{-2} day^{-1}) in NPRT in the
Northwest Pacific.

961

962
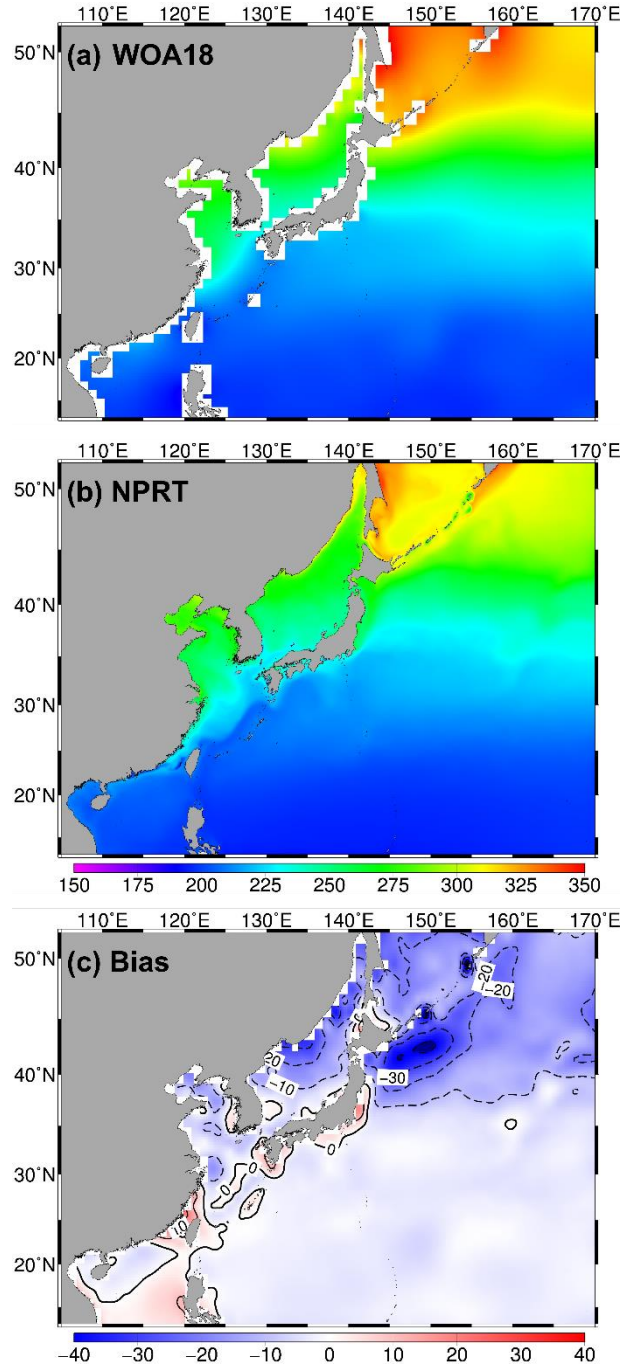
Fig. 17. Horizontal distributions of the annual mean surface dissolved oxygen (DO) concentration (μmol kg^{-1}) in (a) WOA18 and (b) NPRT, and (c) bias between NPRT and WOA18.

966

967
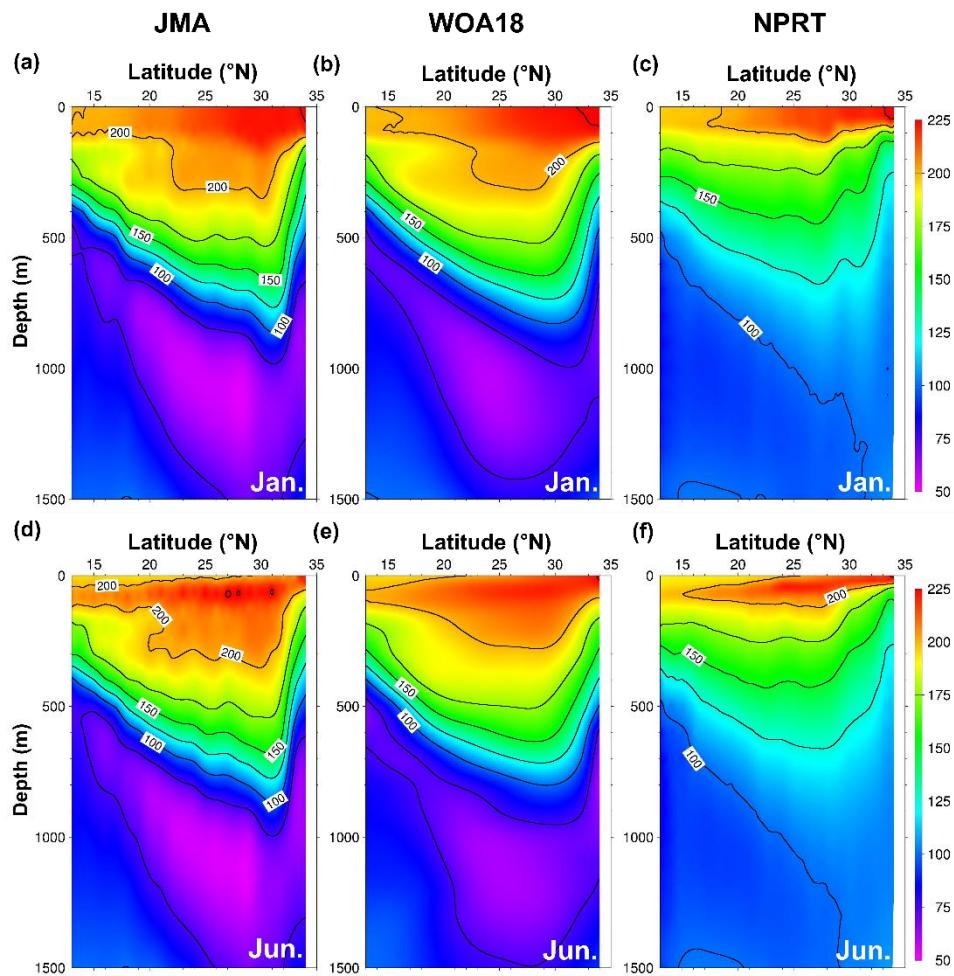
968   **Fig. 18.** Vertical structures of the annual mean dissolved oxygen (DO) concentration (μmol kg⁻

969   ¹) along 137° E line from (a, d) JMA and (b, e) WOA18, and (c, f) NPRT in January (top)

970   and June (bottom).

971

972

973

974   **Table1.** CMIP6 Earth system models were used in this study for comparison with chlorophyll concentration.

Month	Subtropical Region			Subarctic Region			East Sea			YECS		
	NO_3	PO_4	Silicate	NO_3	PO_4	Silicate	NO_3	PO_4	Silicate	NO_3	PO_4	Silicate
1	0.93	1.04	1.77	3.02	2.38	3.44	3.54	3.53	3.32	2.18	1.93	9.54
2	1.36	0.67	2.08	2.77	2.70	3.28	3.70	2.76	5.91	2.93	4.13	13.58
3	1.27	1.22	1.87	2.73	2.82	3.62	2.40	2.29	3.09	2.33	2.53	9.99
4	1.93	1.53	1.74	2.73	2.66	3.86	2.04	1.32	2.59	2.76	1.67	12.77
5	0.79	0.70	1.22	3.44	3.19	3.76	1.83	1.12	2.99	2.93	1.46	5.40
6	1.30	1.68	1.37	3.02	3.58	4.26	2.70	2.63	3.23	3.02	1.80	10.36
7	1.95	2.55	2.10	3.12	3.57	4.23	3.04	2.88	3.44	2.93	2.23	8.58
8	2.49	2.95	2.31	3.27	3.41	4.19	2.97	2.38	4.18	2.78	2.73	10.23
9	2.46	2.60	2.53	2.91	3.41	3.88	2.94	3.29	4.71	2.29	2.26	14.29
10	1.33	1.66	2.15	2.81	3.02	3.57	2.46	2.07	3.99	2.73	2.16	14.36
11	3.97	1.10	1.70	2.61	2.67	4.00	2.03	1.80	3.34	2.09	2.95	13.29
12	4.64	1.86	0.94	2.21	2.47	3.38	3.28	4.42	3.32	2.79	3.76	11.21
13	1.30	0.79	1.40	3.07	3.17	4.19	2.67	2.56	3.68	2.12	2.16	12.61

975

976 **Table2.** CMIP6 Earth system models were used in this study for comparison with chlorophyll concentration.

Model#	Model name	Model center	Physical/Biochemistry model	Data description
1	ACCESS-ESM1-5	CSIRO	MOM5 / WOMBAT	
2	CanESM5	CCCma	NEMO3.4.1 / CMOC	
3	CESM2	NCAR	POP2 / MARBL	
4	CESM2-WACCM	NCAR	POP2 / MARBL	depth-averaged data
5	CESM2-WACCM-FV2	NCAR	POP2 / MARBL	
6	CMCC-ESM2	CMCC	NEMO3.6 / BFM5.2	
7	MPI-ESM1-2-HR	MPI-M	MPIOM1.63 / HAMOCC6	
8	MPI-ESM1-2-LR	MPI-M	MPIOM1.63 / HAMOCC6	
9	CanESM5-1	CCCma	NEMO3.4.1 / CMOC	
10	EC-Earth3-CC	EC-Earth-Consortium	NEMO3.6 / PISCES v2	
11	MPI-ESM-1-2-HAM	HAMMOZ-Consortium	MPIOM1.63 / HAMOCC6	Surface data
12	NorESM2-LM	NCC	MICOM / HAMOCC	
13	NorESM2-MM	NCC	MICOM / HAMOCC	

977

978 **Table 3.** Summary of the Taylor diagram scores for annual mean surface chlorophyll concentrations in
979 the subtropical and subarctic regions, East Sea, and the Yellow and East China Sea (YECS) in
980 NPRT, each ensemble model in CMIP6, GFDL–ESM2M and GFDL–ESM2G. The subarctic
981 (subtropical) region is north (south) of 40° N in the NWP.

Model	Subtropical Region	Subarctic Region	East Sea	YECS
NPRT	1.21	1.64	1.88	2.32
ACCESS-ESM1-5	2.44	3.36	3.07	2.78
CanESM5	2.48	2.71	3.33	2.72
CESM2	1.77	2.47	2.98	2.62
CESM2-WACCM	1.90	2.70	2.96	2.65
CESM2-WACCM-FV2	1.74	2.56	2.92	2.66
CMCC-ESM2	2.72	2.84	3.29	2.79
MPI-ESM1-2-HR	4.32	2.20	3.01	2.58
MPI-ESM1-2-LR	5.77	3.19	2.98	2.73
CanESM5-1	2.13	3.42	3.09	3.50
EC-Earth3-CC	1.60	2.27	2.76	2.27
MPI-ESM-1-2-HAM	2.33	3.29	3.02	3.78
NorESM2-LM	2.22	2.21	2.82	2.60
NorESM2-MM	2.39	2.39	2.81	2.68
GFDL-ESM2M	2.96	4.80	3.06	3.06
GFDL-ESM2G	3.02	3.53	2.73	3.43

982

983

984

985

[Supplementary Figures]
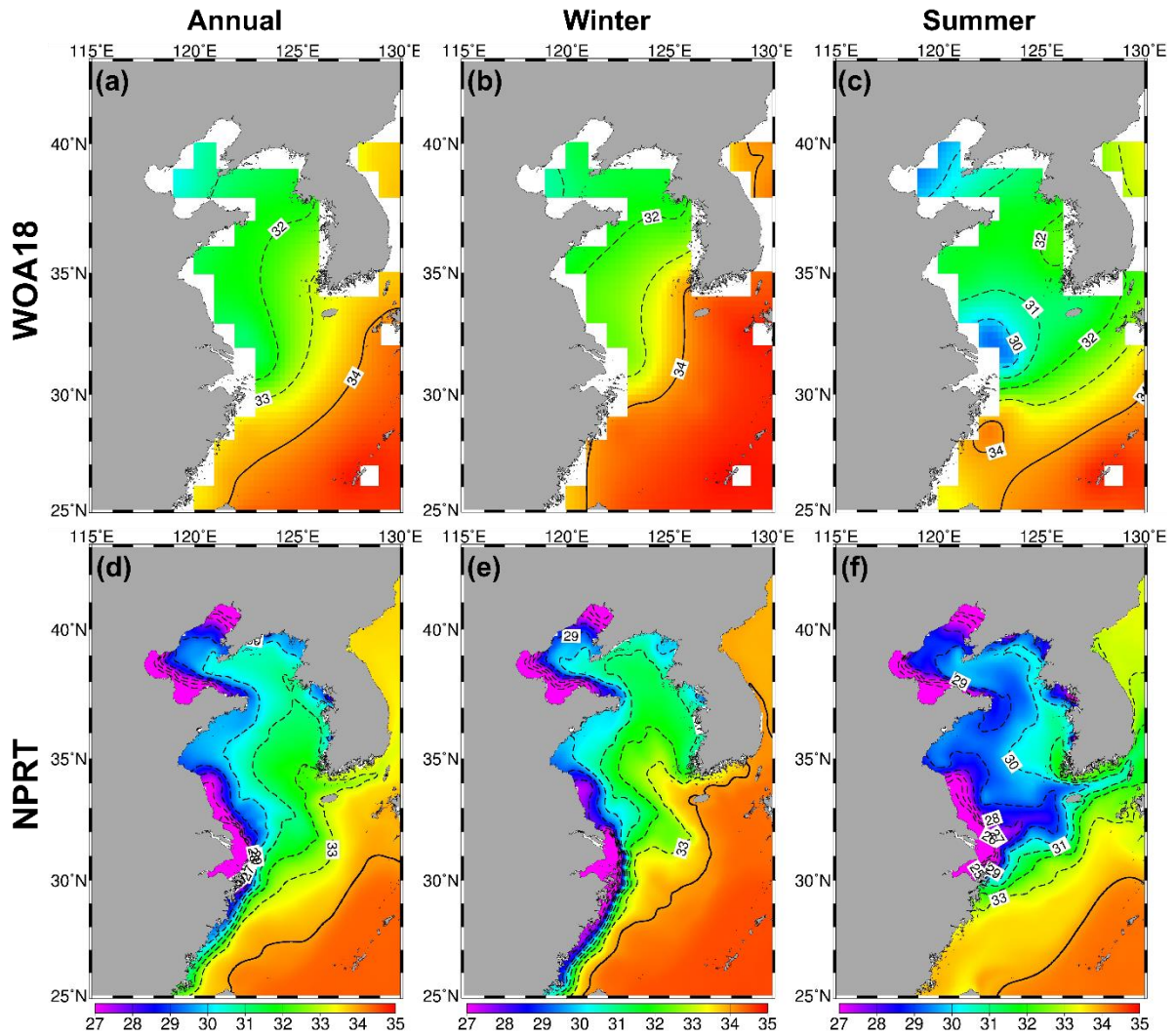
Supplementary Figure S1. Distributions of the surface salinity in (a, b, c) the WOA18 data and (d, e, f) NPRT for (a, d) the annual mean, (b, e) winter and (c, f) summer in the YECS. The thick solid line indicates 34.0 psu and the contour interval is 0.5 psu.

992
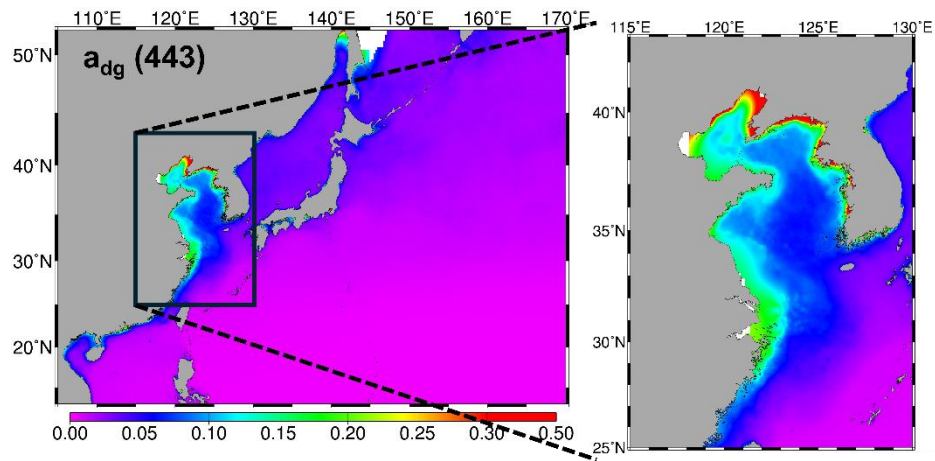
993 **Supplementary Figure S2.** Distributions of the climatological mean absorption coefficient of
994 light for colored detrital matter a_{dg} (443) (unit: m^{-1}) from 2005 to 2014 derived from the
995 MODIS data.

996

997

998

999

1000

1001

1002

1003

1004
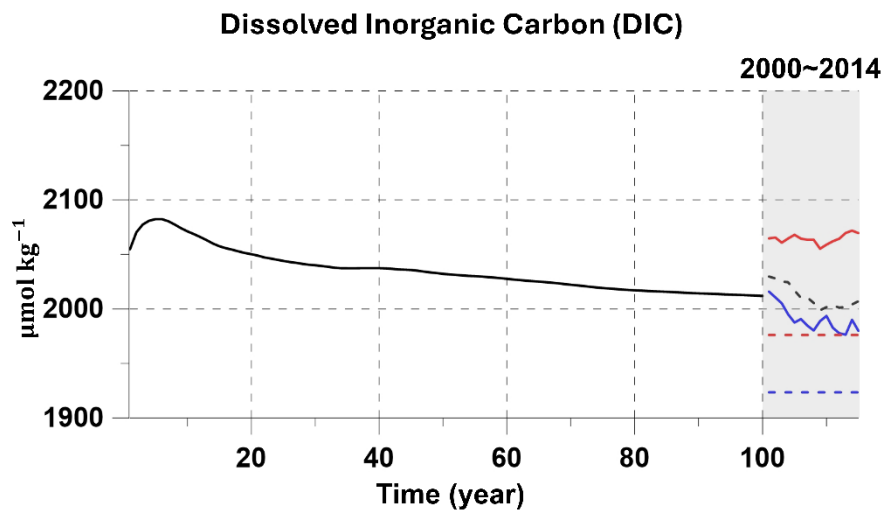
1005 **Supplementary Figure S3.** Time series of the annual mean surface DIC concentration (µmol

1006 kg^{-1}) in the NWP (the subtropical and subarctic regions) during spin-up time using MOM5–

1007 TOPAZ. The spin-up process for the first 100 years (black solid line) was conducted under

1008 a pCO$_2$ (369.6 ppm) and atmospheric forcings (ERA5) conditions of the year 2000. The

1009 MOM5-TOPAZ model was then run for the period 2000–2014 (black dashed line; light gray

1010 shaded region), using the final time step of the 100-year spin-up as the initial condition.

1011 Through these spin-up process, the initial and boundary conditions for the biogeochemical

1012 variables required to conduct NPRT were obtained. The red and blue solid lines (dashed lines)

1013 represent the zonal-averaged surface DIC concentration applied to NPRT (from GLODAPv2)

1014 at the eastern and southern boundary conditions, respectively.